Exact Eddy-Viscosity Equation for Turbulent Wall Flows - Implications for Computational Fluid Dynamics Models

Emmanuel Plaut*
Université de Lorraine, CNRS, LEMTA, F-54000 Nancy, France

Stefan Heinz†
Mathematics Department, University of Wyoming, Laramie, WY, USA !

For turbulent channel flow, pipe flow and zero-pressure gradient boundary layer, Heinz (2018, 2019) yields analytical formulas for the eddy-viscosity ν_t as a product of a function of y^+ (the wall-normal distance scaled in inner units) and a function of y/δ (the same scaled in outer units). By calculating the eddy-viscosity turbulent diffusion term, we construct for those flows an exact high-Reynolds number ν_t equation with one production and two dissipation terms. One dissipation term is universal, peaks near the wall, and scales mainly with y^+. The second, smaller one, is flow-dependent, peaks in the wake, and scales mainly with y/δ. The production term is flow-dependent, peaks in between, and scales similarly. The universal dissipation term implies a length scale analogous to the von Karman length scale used in the SAS models of Menter. This length scale also appears in the production term. This confirms the relevance of these length scales. An asymptotic analysis of all terms in the ν_t budget in the limit of infinite Reynolds numbers is provided. This yields a test bench of existing RANS models with a similar ν_t equation. We show that some models, e.g. the one of Spalart & Allmaras, do not respect the flow physics: they display a production peak in the near-wall region. We modify the most promising model, a SAS model. As a step forward towards a solution to the wall damping problem, the ν_t equation of our model behaves much more correctly in the near-wall region.

I. Introduction

Reynolds-Averaged Navier-Stokes (RANS) models are still widely used in Engineering Computational Fluid Dynamics (CFD, [1, 2]), because they allow studies in complex setups for a lower computational cost than more sophisticated methods like Large Eddy Simulations (LES) or Hybrid methods [3]. Among RANS models, two-equations models like the $k-\omega$ [4, 5] and $k-\epsilon$ [6] models are popular. Their equation for the turbulent kinetic energy k is known to be rather accurate. Indeed, its high-Reynolds number form can be validated with direct numerical simulations (DNSs - we use those of [7]) in channel flows, out of the viscous and buffer layers, as shown in the appendix A. On

*Professor, Collégium Lorraine INP, Mines Nancy. Corresponding author, emmanuel.plaut@univ-lorraine.fr .
†Professor, Department of Mathematics, AIAA Associate Fellow.

Submitted 30 March 2021; published online 13 December 2021; AIAAJ vol. 60, No 3, March 2022; https://doi.org/10.2514/1.J060761

the contrary, the equations for the turbulent dissipation ϵ or the turbulent frequency ω of these models are much less accurate, as shown, with the same DNS data, in the appendix B. These problems are related to the fact that these equations have been constructed empirically on phenomenological and dimensional bases. Alternate RANS models where one field is the eddy-viscosity ν_t itself, which evolves according to its own equation, look appealing since ν_t is doubtless a quite relevant variable. The first models of this kind also constructed the ν_t equation on phenomenological and dimensional bases [8–10], or from the $k-\epsilon$ model itself, with a supplementary equation (the Townsend's relation), in the case of [11]. However, there have been recently attempts to use more systematic approaches [12, 13]. The Scale-Adaptive Simulation (SAS) models of [14, 15] are also $k-\nu_t$ models, which are more phenomenological than the ones of [12, 13], but may work as Hybrid RANS-LES models. Their ν_t equation implies, through the so-called von Karman length scale ℓ_{vK} , the second gradient of the mean velocity, which renders them 'instability-sensitive': in highly non-homogeneous flows the second gradient of the mean velocity, in the denominator of ℓ_{vK} , increases, hence ℓ_{vK} decreases, hence the corresponding dissipation term increases, hence ν_t decreases. This allows resolved motions in unsteady simulations. Relevant applications of variants of this model to quite complex flows are for instance presented in [14, 16, 17]. Reference [18] also proposed an interesting extension of the SAS approach under the form of a Reynolds stress model.

The facts that many variants of the SAS models exist, and that their equations are built on phenomenological grounds, raise however theoretical questions. Accordingly, it is noticeable that the more systematic approaches of [12, 13] are quite different: whereas [12] started from a conventional Reynolds stress model, [13] started from the nonlocal analysis presented in [19]. Obviously, there is no perfect way to analytically derive the ν_t equation.

The aim of this work is to offer a third way, at least for a relevant class of flows: fully developed channel and pipe flows, together with zero-pressure gradient boundary layers over a flat plate. For these three canonical flows, denoted hereafter 'turbulent wall flows', [20, 21] proposed analytic models of the mean flow U, Reynolds shear stress $-\langle u_x u_y \rangle$ and eddy viscosity ν_t , built after a thorough analysis of recent DNS, including those of [7, 22, 23], and experimental data, for instance those of [24]. Interestingly, these models are valid for friction-based Reynolds numbers $Re_\tau \gtrsim 500$: the limit $Re_\tau \to \infty$ is included. Our approach, see Eq. (11), is then to analytically calculate the turbulent diffusion of ν_t and to identify the opposite of this as the sum of a positive production term minus positive dissipation terms. The fact that these terms are analytical offers a better intellectual understanding of the ν_t equation, and also a practical understanding of the scaling properties of all terms in this equation. This also permits an accurate description of the limit case $Re_\tau \to \infty$. Another goal is the creation of a basis for the numerical and physical evaluation of existing models. This is exemplified on the study of the models [10, 12, 14, 15]. Regarding the SAS models, we assume that, for the attached flows studied, they work in steady RANS mode. We finally derive a promising modification of one SAS model. In particular, it behaves much more correctly in the near-wall region.

In Sec. II, we offer a presentation and physical analysis of our model, which considers only high-Reynolds number turbulent wall flows with $Re_\tau \gtrsim 500$. The physical questions that we want to answer concern the scalings of the production and dissipation terms in the ν_t equation, and the effects of the flow cases and Reynolds number. Asymptotic formulas valid in the limit $Re_\tau \to \infty$, for all terms in the ν_t equation, either in the near-wall region (y^+ scaling) or in the outer region (y/δ scaling), are in particular given in the Secs. II.F and II.G. An overview of all our physical results is offered in the Sec. II.H, where the differences between the eddy-viscosity budget thus obtained and the known turbulent kinetic energy budget are stressed. All this yields a test bench of existing models that imply a ν_t equation with a standard turbulent diffusion or transport term (T_ν in equation 11). This test bench is used in the Secs. III.A to III.C to evaluate three such models: the models of [10, 12] and the SAS models of [14, 15], which have some variants. Finally, the mathematical and physical knowledges gained, and our test bench, are used to propose a new SAS model in Sec. III.D. We conclude in Sec. IV.

II. Analysis: exact eddy-viscosity formula and transport equation

A. Turbulent wall flows - Exact eddy-viscosity formula

Following [20, 21], we consider turbulent wall flows of incompressible fluids of mass density ρ and kinematic viscosity ν. Locally, a cartesian system of coordinates Oxyz is used, such that x points in the streamwise direction, and y measures the distance to the closest wall. Neglecting small normal mean velocities in the boundary-layer case, one considers that to leading order the mean flow

$$\mathbf{U} \;=\; U(y)\;\mathbf{e}_x \tag{1}$$

with $\mathbf{e}_x$ the unit vector in the x-direction. A relevant quantity is the mean strain rate

$$S \;=\; \partial U/\partial y\;. \tag{2}$$

The macroscopic length scale δ is the half-channel height, pipe radius, or 99% boundary layer thickness with respect to channel flow, pipe flow, and boundary layer, respectively. Denoting $u_x\mathbf{e}_x + u_y\mathbf{e}_y + u_z\mathbf{e}_z$ the fluctuating velocity, the RANS eddy viscosity may be defined exactly as

$$\nu_t = -\left\langle u_x u_y \right\rangle / S \tag{3}$$

where the angular brackets denote the Reynolds average. The mean wall shear stress τ_w is used to define the friction velocity $u_\tau = \sqrt{\tau_w/\rho}$. From this wall or inner units are defined: $y^+ = u_\tau y/\nu,\; U^+ = U/u_\tau$ and

$$S^+ \;=\; \partial U^+/\partial y^+\;. \tag{4}$$

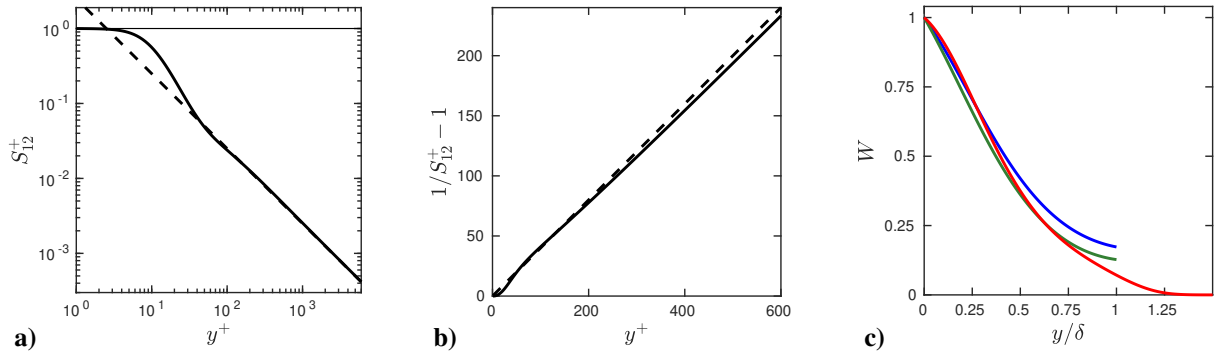

Fig. 1 Exact model. a) Continuous curve: S_{12}^+ , dashed line: $1/(\kappa y^+)$. b) Continuous curve: $1/S_{12}^+ - 1$, dashed line: κy^+. c) W for channel (blue), pipe (green), boundary layer (red).

Finally, the friction-velocity Reynolds number $Re_\tau = \delta^+ = u_\tau \delta/\nu$. In Eq. (11) of [21], an analytic expression is proposed for the normalized eddy viscosity, which is valid as soon as the Reynolds number $Re_\tau \gtrsim 500$,

$$\nu^+ = \nu_t/\nu = (1/S_{12}^+ - 1)\, W\,. \tag{5}$$

There $S_{12}^+ = S_1^+ + S_2^+$ is the inner flow contribution to the dimensionless mean strain rate S^+ (4), disregarding wake effects, see Eq. (7) of [20] and the corresponding discussion. Precisely, the universal function

$$S_{12}^+ = S_{12}^+(y^+) = 1 - \left[\frac{(y^+/a)^{b/c}}{1+(y^+/a)^{b/c}}\right]^c + \frac{1}{\kappa y^+}\frac{1+h_2/(1+y^+/h_1)}{1+y_k/(y^+H)}\,, \tag{6}$$

with $a = 9,\ b = 3.04,\ c = 1.4,\ H = H(y^+) = (1+h_1/y^+)^{-h_2}$, $h_1 = 12.36,\ h_2 = 6.47,\ y_k = 75.8$, and the von Karman constant

$$\kappa = 0.40\,. \tag{7}$$

The function S_{12}^+ , plotted on the Fig. 1a, approaches naturally 1 as $y^+ \to 0$ in the viscous sublayer. On the contrary, as $y^+ \to \infty$, $S_{12}^+ \sim 1/(\kappa y^+)$, in agreement with the log law. Therefore the function $1/S_{12}^+ - 1$, plotted on the Fig. 1b, which appears in the eddy viscosity (5), vanishes in the limit $y^+ \to 0$, and then increases smoothly to approach the function κy^+ as $y^+ \to \infty$.

The second ingredient of the theory is the function W, which is flow-dependent and in outer scaling, because it describes wake effects. With the notations of [20, 21], $W = 1/G_{CP}$ for channel and pipe flows, M_{BL}/G_{BL} for boundary layers, where G_{CP} and G_{BL} characterize the wake contribution S_3^+ to the dimensionless mean strain rate S^+ (see Eqs. 7 and A.22 of [20]), M_{BL} characterizes the total stress in boundary layers (see Eq. 4 of [21]). For channel and pipe flows

$$W = W_X(y/\delta) \quad \text{with} \quad W_X(y) = \frac{K_X y + (1-y)^2(0.6y^2+1.1y+1)}{1+y+y^2(1.6+1.8y)}\,, \tag{8}$$

$X = C,\ K_C = 0.933$ for channel, $X = P,\ K_P = 0.687$ for pipe; for boundary layers

$$W \ = \ W_{BL}(y/\delta) \quad \text{with} \quad W_{BL}(y) \ = \ \frac{1 + 0.285\ y\ e^{y(0.9+y+1.09y^2)}}{1 + (0.9 + 2y + 3.27y^2)y}\ \ e^{-y^6-1.57y^2}\ . \tag{9}$$

The wake function W is plotted for these three flows on the Fig. 1c. In the near-wall region, when $y/\delta \to 0,\ W \to 1$, hence the eddy viscosity (5), $\nu^+ \ = \ (1/S^+_{12}(y^+) - 1)\ W(y^+/\delta^+) \ \sim \ (1/S^+_{12}(y^+) - 1)$. Therefore the log-layer eddy viscosity κy^+ is approximately recovered if $1 \ll y^+ \ll \delta^+$; for a more precise discussion, see Sec. 4.1 of [21]. When y becomes of the order of δ, wake effects come in, that saturate the growth of the eddy viscosity (5), since W decreases. The maximum value of y is δ in channel and pipe flows: if $y \in [\delta, 2\delta]$ the mean fields can be obtained by symmetries from the mean fields for $y \in [0, \delta]$. On the contrary, y may be much larger in boundary layers. Naturally, $W_{BL} \to 0$ as $y \to \infty$; precisely $W_{BL} < 10^{-3}$ as soon as $y > 1.36\delta$.

The ν_t model (5) has been validated by a study of DNS and experimental data. For instance, Figs. S.6abc of the supplementary material to [21] show the eddy viscosity of various DNSs, one for each canonical flow, compared with two variants of the eddy-viscosity model (5). In particular, the magenta curves show $\nu^+ = \kappa y^+\ W$ with our notations, i.e. $(1/S^+_{12} - 1)$ in (5) has been replaced by κy^+. The agreement with the DNS is good, except in the outer region, where in (3) both the numerator $\langle u_x u_y \rangle$ and the denominator S tend to zero, hence the DNS noise is amplified. A direct comparison between the ν_t model (5) and channel flow DNS is displayed on our Figs. 14bc.

B. Exact eddy-viscosity equation for turbulent wall flows

Since the focus of our study is on high-Reynolds numbers wall-bounded flows, we assume that the eddy-viscosity equation takes the standard form

$$\sigma \frac{\partial \nu_t}{\partial t} \ = \ \frac{\partial}{\partial y}\Big(\nu_t \frac{\partial \nu_t}{\partial y}\Big) \ + \ P_\nu \ - \ D_\nu \tag{10}$$

with $P_\nu > 0$ the production, $D_\nu > 0$ the dissipation term. The dimensionless coefficient σ, of order 1, which is a 'turbulent Prandtl number', plays no role in the turbulent wall flows, where the mean fields are steady, but is kept in (10) for the sake of comparison with existing turbulence models. In turbulent wall flows, according to (10), the opposite of the turbulent diffusion term or transport term reads

$$-T_\nu \ = \ -\frac{\partial}{\partial y}\Big(\nu_t \frac{\partial \nu_t}{\partial y}\Big) \ = \ P_\nu \ - \ D_\nu\ . \tag{11}$$

A calculation of T_ν starting from (5) leads to $D_\nu = D_{\nu i} + D_{\nu o}$ with

$$D_{\nu i} = \kappa^2 \frac{\nu_t^2}{L_{\nu K}^2} \frac{1}{f^2}, \tag{12a}$$

$$P_\nu = \kappa \frac{\nu_t^2}{L_{\nu K}\,\delta} \frac{1}{1 - S_{12}^+} \left(- \frac{4W'}{W} \right) = \kappa \frac{\nu\,\nu_t}{L_{\nu K}\,\delta} \frac{1}{S_{12}^+} (-4W'), \tag{12b}$$

$$D_{\nu o} = \frac{\nu_t^2}{\delta^2} \frac{W'^2 + WW''}{W^2} = \frac{\nu^2}{\delta^2} (1/S_{12}^+ - 1)^2 (W'^2 + WW''). \tag{12c}$$

The indices i and o refer to 'inner' and 'outer' terms, respectively, and the notation $D_{\nu o}$ is slightly improper since this term is slightly negative in the near-wall region. However, $D_{\nu o}$ is much smaller in this region than in the outer region where it peaks, as it will be shown in the Fig. 5ab for channel flow, 6ab for pipe flow, 7ab for boundary layers. Moreover $D_\nu = D_{\nu i} + D_{\nu o} > 0$ everywhere, as it will be shown in the Figs. 5cd for channel flow, 6cd for pipe flow, 7cd for boundary layers, hence the notation D_ν is fully justified.

In addition to the functions S_{12}^+ and W defined in Sec. II.A, there appear in Eqs. (12) other functions that are built on these. The first one is the asymptotic von Karman length scale

$$L_{\nu K} = \kappa \left| \frac{S_{12}}{\partial S_{12}/\partial y} \right| \quad \text{or} \quad L_{\nu K}^+ = \kappa \left| \frac{S_{12}^+}{\partial S_{12}^+/\partial y^+} \right|. \tag{13}$$

It is defined as the von Karman length scale used by the SAS models

$$\ell_{\nu K} = \kappa \left| \frac{S}{\partial S/\partial y} \right|, \tag{14}$$

but replacing S by S_{12} , i.e., disregarding 'wake effects'. The fact that the length scale $L_{\nu K}$ appears in (12a) and (12b) confirms on very firm bases the relevance of this length scale, which was conjectured by [14, 15]. Only the inner-units $L_{\nu K}^+(y^+)$ is universal, whereas in outer units $L_{\nu K}(y)/\delta$ has to be calculated as $L_{\nu K}^+/\delta^+$ at $y^+ = \delta^+(y/\delta)$: it depends on $\delta^+ = Re_\tau$. Since, as $y^+ \to \infty$, in agreement with the log law, $S_{12}^+ \sim 1/(\kappa y^+)$, $L_{\nu K}^+ \sim \kappa y^+$, as confirmed by the Fig. 2a. The functions $\ell_{\nu K}^+(y^+)$ (Fig. 2a) or $\ell_{\nu K}(y/\delta)$ (Fig. 2b), that depend on the flow case and Reynolds-number, have been computed using the accurate expressions of S^+ of the equation (7) of [20], that take into account wake effects. In channel or pipe flow, U peaks at the centerplane or pipe axis $y = \delta$, hence S and $\ell_{\nu K}$ vanish there. On the contrary, in boundary layer flow, S and $\ell_{\nu K}$ vanish only in the limit $y \to \infty$. Phenomenologically, $L_{\nu K}$ and $\ell_{\nu K}$ become large in the viscous sublayer, because there the velocity profile becomes linear ($U \propto y$), then they diminish in the buffer layer where there are strong gradients; further away in the outer region $L_{\nu K}$ and $\ell_{\nu K}$ again become large because the velocity profile flattens. The wake effects finally saturate the growth of $\ell_{\nu K}$ and even impose a decrease of $\ell_{\nu K}$, as already explained, but do not influence $L_{\nu K}$. The Fig. 2c suggests that, because the dimensional factor in $D_{\nu i}$ (12a),

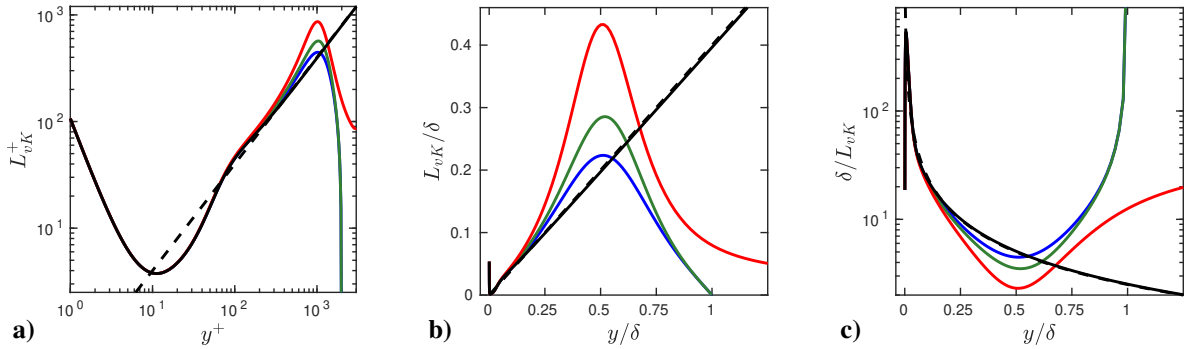

Fig. 2 Exact model. All curves start at $y^+ = 1$. a,b) The asymptotic von Karman length scale $L_{\nu K}$ (black continuous); its log law approximation κy (black dashed); the von Karman length scale $\ell_{\nu K}$ for channel (blue), pipe (green), boundary layer (red). The $\ell^+_{\nu K}$ curves of the Fig. a and all curves of the Fig. b are computed at $Re_\tau = 1995$. The Fig. c shows the same curves as Fig. b but with the inverse ordinates and linear-log scales.

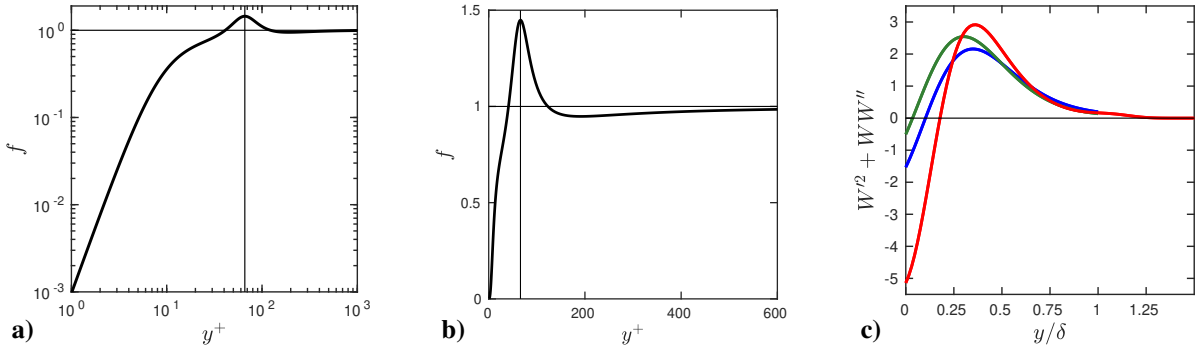

Fig. 3 Exact model. a,b) The damping function f. The vertical lines mark $y^+ = 66$. c) The function $W'^2 + WW''$ for channel (blue), pipe (green), boundary layer (red).

P_ν (first expression in 12b) and $D_{\nu o}$ (first expression in 12c) are respectively $\nu_t^2/L_{\nu K}^2$, $\nu_t^2/(L_{\nu K}\delta)$ and ν_t^2/δ^2, in the ratii $\delta^2/L_{\nu K}^2$, $\delta/L_{\nu K}$, 1, those will peak in the inner, intermediate and outer regions. This will be confirmed in the Figs. 5 for channel flow, 6 for pipe flow, 7 for boundary layers.

Another ingredient in $D_{\nu i}$ (12a) is the universal damping function

$$f \;=\; f(y^+) \;=\; (1 - S^+_{12}) \left(\frac{(S^+_{12} - 1)\; S^+_{12}\; d^2 S^+_{12}/dy^{+2}}{(dS^+_{12}/dy^+)^2} + 3 - 2S^+_{12} \right)^{-1/2} . \tag{15}$$

It is plotted on the Figs. 3ab. It does tend to zero as $y^+ \to 0$ and 1 as $y^+ \to \infty$.

Finally, in P_ν (12b) and $D_{\nu o}$ (12c) the rightmost functions depend only on W and its derivatives. In P_ν there appears $-4W'$ which is positive according to the Fig. 1c, hence $P_\nu > 0$ as required. In $D_{\nu o}$ there appears $W'^2 + WW''$ which is plotted on the Fig. 3c. The function $W'^2 + WW'' > 0$ except in a more or less narrow near-wall region, depending on the flow case: this impacts the sign of $D_{\nu o}$ as already discussed after the Eqs. (12).

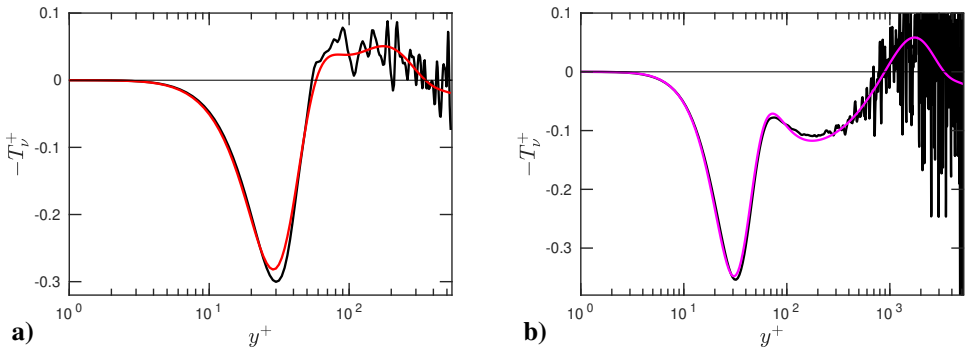

Fig. 4 DNS and exact model for channel flows. Black curve: the opposite of the dimensionless transport term $-T_\nu^+$ (16) computed with the DNS of [7] at $Re_\tau = 543$ (a), 5186 (b). Colored curve: the same term computed with our model (17).

C. The channel flow case

In typical channel flow cases, a comparison of the opposite of the dimensionless transport term

$$-T_\nu^+ = -\frac{\partial}{\partial y^+}\left(\nu^+\frac{\partial v^+}{\partial y^+}\right) = -\frac{T_\nu}{u_\tau^2} \tag{16}$$

computed with finite differences from two DNSs of [7] and its model (11,12),

$$-T_\nu^+ = P_\nu^+ - D_\nu^+ = -D_{\nu i}^+ + P_\nu^+ - D_{\nu o}^+ \tag{17}$$

is shown on the Figs. 4. Except in the outer region, where the DNS noise is amplified, there is a good agreement between the model and the DNS, especially for the highest Reynolds number case.

The separation of $-T_\nu^+$ into the three terms of the model, $-D_{\nu i}^+$, P_ν^+ and $-D_{\nu o}^+$, is illustrated on the Figs. 5. The Figs. 5a, c and g show that the dissipation term $D_{\nu i}^+$ dominates in the near-wall region. In this region, and in inner scalings, $-D_{\nu i}^+(y^+)$, $-D_\nu^+(y^+)$ and $-T_\nu^+(y^+)$ approach as $Re_\tau \to \infty$ a limit profile $-D_{\nu ia}^+$, which is plotted in black, and will be studied in the Sec. II.F. A plateau around $y^+ \simeq 400$ and

$$D_{\nu i}^+ \simeq D_\nu^+ \simeq T_\nu^+ \simeq \kappa^2$$

builds up as $Re_\tau \to \infty$, in agreement with the formula for the log-layer normalized eddy viscosity, $\nu^+ = \kappa y^+$. For larger values of y/δ, after this plateau, the Figs. 5bdfh show that all terms, considered in inner-outer scalings, $-D_{\nu i}^+(y/\delta)$, $-D_{\nu o}^+(y/\delta)$, $-D_\nu^+(y/\delta)$, $P_\nu^+(y/\delta)$ and $-T_\nu^+(y/\delta)$, approach limit profiles as $Re_\tau \to \infty$. These limit profiles, plotted in black for the three latest functions, denoted $-D_{\nu a}^+$, $P_{\nu a}^+$ and $-T_{\nu a}^+$, will be studied in the Sec. II.G.

D. The pipe flow case

In the eddy-viscosity formula (5), the only difference between channel and pipe flows is described by the change of the coefficient K_X in the function W_X (8) that contains the wake effects. This change from $K_C = 0.933$ to $K_P = 0.687$ is moderate, therefore the transport term and its contributions are close to the ones of channel flow, as shows the comparison between Figs. 5 and 6. All the comments made on Figs. 5 at the end of Sec. II.C also apply to Figs. 6.

E. The boundary layer case

The boundary layer case differs from the channel and pipe flow cases in that the maximum value of y (resp. y^+) is not δ (resp. $\delta^+ = Re_\tau$) but, in principle, infinity. Moreover, the wake function W_{BL} of boundary layers (9) differs significantly from the one of channel and pipe flows (8). The comparison of Figs. 7 with Figs. 5 and 6 shows similar behaviours in the ranges $y \in [0, \delta[$ i.e. $y^+ \in [0, \delta^+[$, whereas there are differences in the outer region. At $y = \delta$, i.e. the centerplane in channels or the pipe axis in pipes, the function T_ν should present a vanishing slope for symmetry reasons, as confirmed by Figs. 5h and 6h; note that the outer term $-D^+_{\nu o}$ plays an important role there. In boundary layers, one does not expect a similar property, but that T_ν should approach 0 as $y \to \infty$. This is what suggests the Fig. 7h, and what would confirm a figure drawn with a larger interval of the abscissas: for all the Reynolds numbers implied, that range from 543 to 80000, $|T^+_\nu| < 10^{-3}$ as soon as $y > 1.32\delta$.

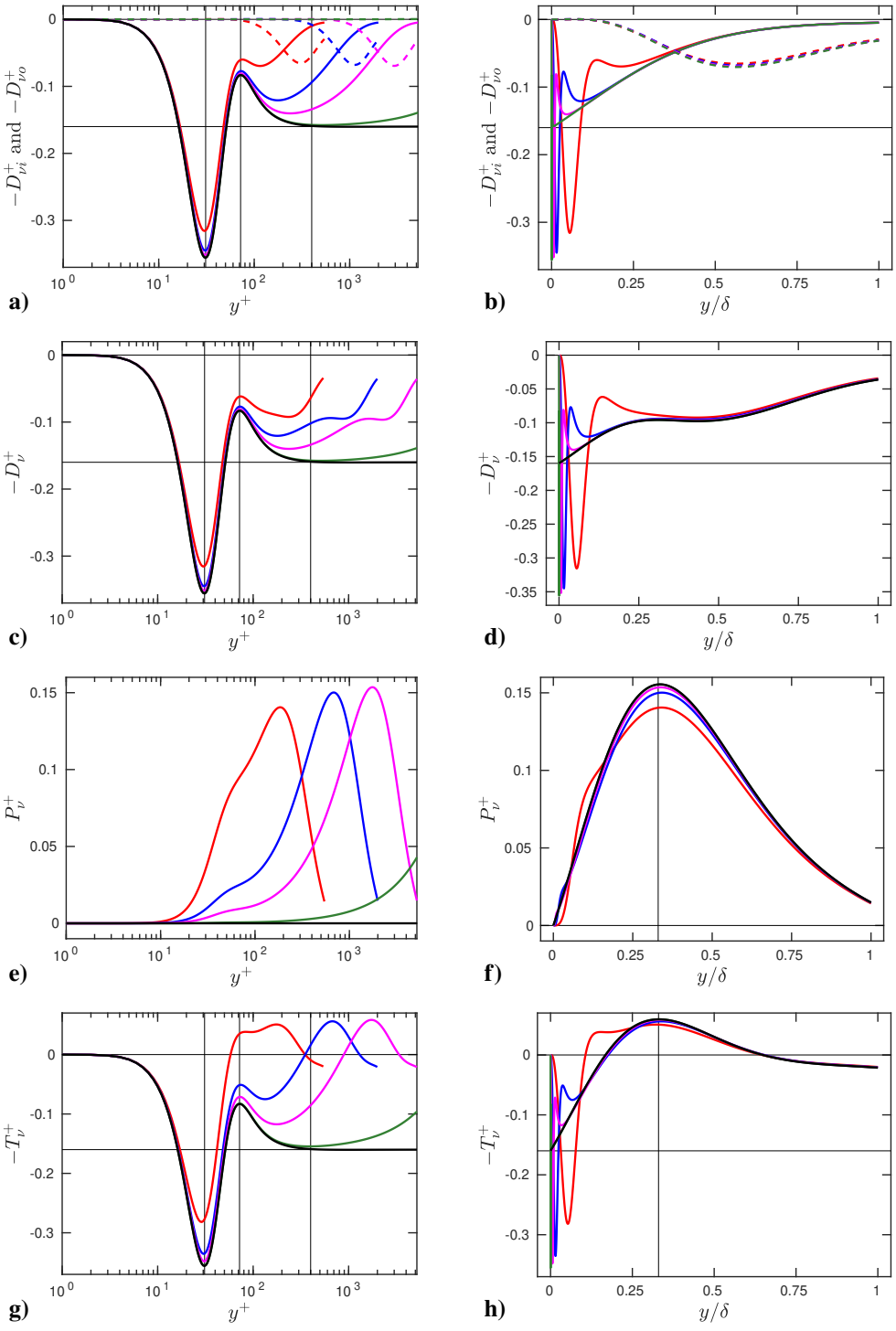

Fig. 5 Exact model for channel flows. The colored curves, at $Re_\tau = 543$ (red), 1995 (blue), 5186 (magenta), 80000 (green), show the various contributions to $-T_\nu^+$ and their sum. a,b) $-D_{\nu i}^+$ (resp. $-D_{\nu o}^+$): continuous (resp. dashed) curves. c,d) $-D_\nu^+$. e,f) P_ν^+ . g,h) $-T_\nu^+$. The black curves show the asymptotic profiles approached as $Re_\tau \to \infty$ either at fixed y^+ in (a,c,g) or fixed y/δ in (d,f,h). a,c,g) $-D_{\nu ia}^+$. d) $-D_{\nu a}^+$. f) $P_{\nu a}^+$. h) $-T_{\nu a}^+$. On (a,c,g) the vertical lines mark $y^+ = 31,\ 72$ and 400; on (f,h) $y = 0.33\delta$. On (a,b,c,d,g,h) the horizontal lines mark $-T_\nu^+ = 0$ and $-\kappa^2$.

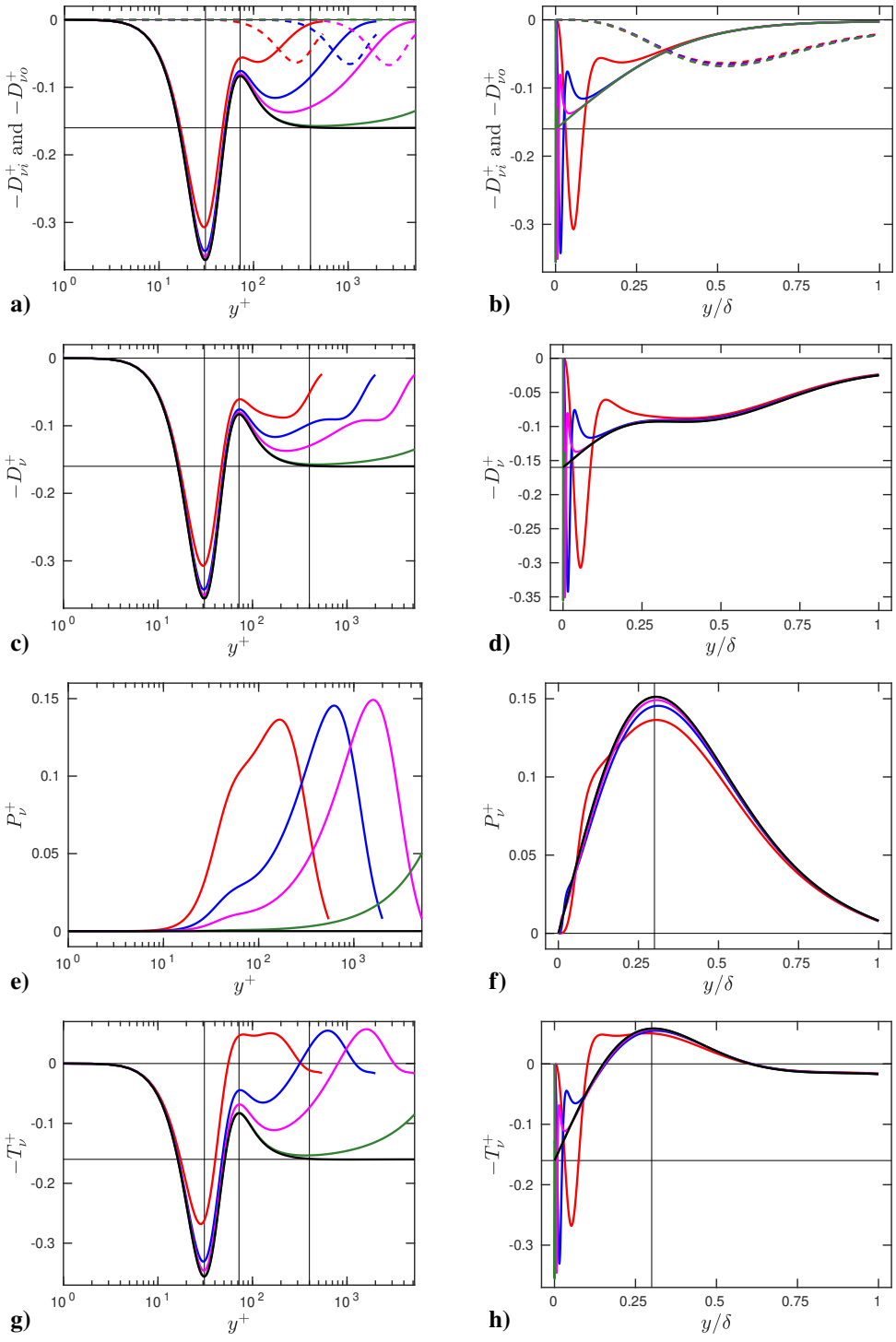

Fig. 6 Same as Fig. 5, but for pipe flows. On (f,h) the vertical lines mark $y = 0.3\delta$.

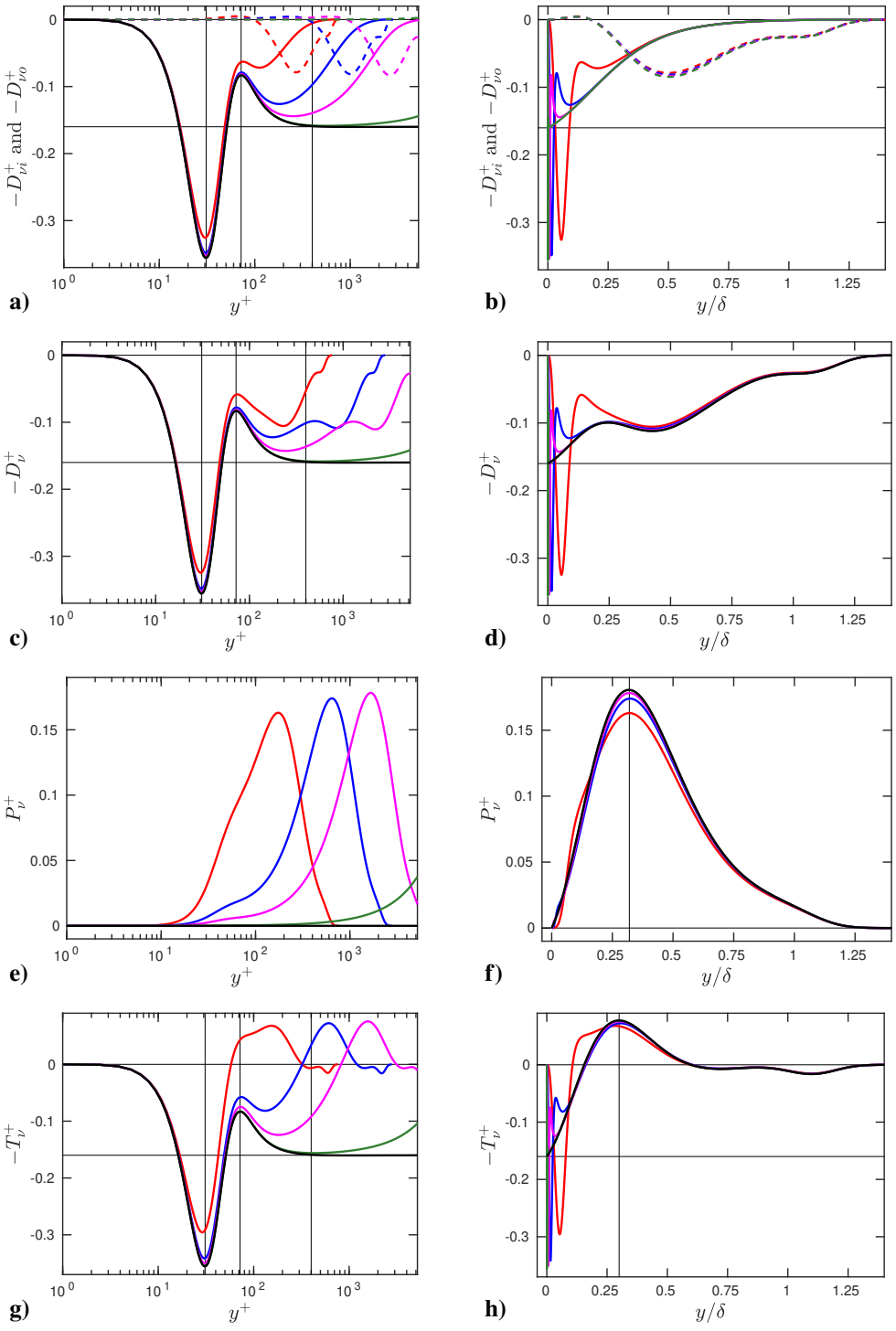

Fig. 7 Same as Fig. 5, but for boundary layers. On (f) the vertical line marks $y = 0.32\delta$, on (h) $y = 0.3\delta$.

F. Asymptotic profiles in the inner region

Figures 5ae, 6ae and 7ae show that, as $Re_\tau \to \infty$, at fixed y^+, $D^+_{\nu o}$ and $P^+_\nu \to 0$. Thus the dissipation term $D_{\nu i}$ dominates in the inner region, and controls the transport term, i.e. $-T_\nu \sim -D_{\nu i}$. Figures 5a, 6a and 7a further show that $D_{\nu i}$ scales with y^+, and approaches in inner units a universal asymptotic profile. This happens because, at fixed y^+, $y/\delta = y^+/Re_\tau \to 0$ as $Re_\tau \to \infty$, hence $W(y/\delta) \to 1$, hence $\nu_t \sim \nu(1/S^+_{12} - 1)$. In physical terms, the wake region goes to infinity in inner scaling. By insertion of this estimate of ν_t in Eq. (12a), one obtains the asymptotic dissipation function

$$D_{\nu ia} = \kappa^2 \frac{\nu^2}{L^2_{\nu K}} \frac{(1/S^+_{12} - 1)^2}{f^2} \quad \text{or} \quad D^+_{\nu ia} = \kappa^2 \frac{(1/S^+_{12} - 1)^2}{L^{+2}_{\nu K}} \frac{1}{f^2} \,. \tag{18}$$

It is universal in that it does not depend on the flow case, but only on S^+_{12} , see the Eqs. (13) and (15). Moreover, $D^+_{\nu ia}$ considered as a function of y^+ also does not depend on Re_τ . The function $-D^+_{\nu ia}$ is plotted in black on Figs. 5acg, 6acg and 7acg. At fixed y^+, when $Re_\tau \to \infty$, both $-D^+_{\nu i}$, $-D^+_\nu$ and $-T^+_\nu$ approach $-D^+_{\nu ia}$. On the Figs. 5acg, 6acg and 7acg, the first vertical line at $y^+ = 31$ indicates the dissipation peak, with $\max D^+_{\nu ia} \simeq 0.36$, the second vertical line at $y^+ = 72$ indicates a local minimum of dissipation, whereas the third vertical line at $y^+ = 400$ indicates the beginning of the log-layer plateau. Indeed, as $y^+ \to \infty$, since $1/S^+_{12} - 1$ and $L^+_{\nu K}$ approach κy^+, whereas $f \to 1$, one has $D^+_{\nu ia} \to \kappa^2$, in agreement with the expression of the log-layer eddy viscosity $\nu^+ = \kappa y^+$. Precisely, $|D^+_{\nu ia} - \kappa^2| < 10^{-3}$ as soon as $y^+ \geq 400$.

G. Asymptotic profiles in the outer region

1. Dissipation

The Figs. 5bd, 6bd and 7bd show that, as $Re_\tau \to \infty$, in the outer region, the dissipation terms $D^+_{\nu i}$, $D^+_{\nu o}$ and their sum D^+_ν scale with y/δ, and approach asymptotic profiles that depend only on the flow case. These profiles are obtained by starting from the expressions (12a) and (12c), transformed in inner units,

$$D^+_\nu = \kappa^2 \frac{\nu^{+2}}{L^{+2}_{\nu K}} \frac{1}{f^2} + \frac{1}{\delta^{+2}} (1/S^+_{12} - 1)^2 \, (W'^2 + WW'') \,. \tag{19}$$

At fixed $y/\delta > 0$, as $Re_\tau \to \infty$, one has $y^+ = Re_\tau \, (y/\delta) \to \infty$, therefore one can replace in (19) the eddy viscosity ν^+, the strain rate S^+_{12} , the von Karman length-scale $L^+_{\nu K}$ and the damping function f by their approximations valid as $y^+ \to \infty$,

$$\nu^+ \sim \kappa y^+ \, W \,, \quad S^+_{12} \sim 1/\kappa y^+ \,, \quad L^+_{\nu K} \sim \kappa y^+ \,, \quad f \sim 1 \tag{20}$$

see the discussions after equations (5-7) for ν^+ and S^+_{12} , equations (13-14) for $L^+_{\nu K}$. This yields the asymptotic profiles

$$D^+_{\nu a} = \kappa^2 \, W^2 + \kappa^2 \left(\frac{y}{\delta}\right)^2 (W'^2 + WW'') \quad \text{or} \quad D_{\nu a} = \kappa^2 \, u_\tau^2 \, W^2 + \kappa^2 \, u_\tau^2 \left(\frac{y}{\delta}\right)^2 (W'^2 + WW'') \,, \tag{21}$$

where the first (resp. second) terms correspond to the asymptotic profile of $D^+_{\nu i}$ or $D_{\nu i}$ (resp. $D^+_{\nu o}$ or $D_{\nu o}$). Since the wake function W depends only on y/δ, see equations (8-9), $D^+_{\nu a}$ is, for a fixed flow case, a function of y/δ only. The functions $-D^+_{\nu a}$ are plotted in black on the Fig. 5d for channel flow, 6d for pipe flow, 7d for boundary layer. At fixed y/δ, they are well approached by $-D^+_\nu$ as $Re_\tau \to \infty$.

2. Production

The Figs. 5ef, 6ef and 7ef show that, as $Re_\tau \to \infty$, the production of the eddy viscosity vanishes in the inner region, scales with y/δ, and approaches in the outer region asymptotic profiles that depend only on the flow case. These profiles are obtained by inserting, in the second expression of P_ν (12b), transformed in inner units,

$$P^+_\nu \;=\; \kappa\,\frac{\nu^+}{S^+_{12}\,L^+_{\nu K}\,\delta^+}\,(-4W')\;, \tag{22}$$

the equivalents of ν^+, S^+_{12} and $L^+_{\nu K}$ given in (20). This yields the asymptotic profiles

$$P^+_{\nu a} \;=\; \kappa^2\,\frac{y}{\delta}\,(-4WW') \quad \text{or} \quad P_{\nu a} \;=\; \kappa^2\,u_\tau^2\,\frac{y}{\delta}\,(-4WW')\;. \tag{23}$$

Similar to $D^+_{\nu a}$ (21), $P^+_{\nu a}$ is, for a fixed flow case, a function of y/δ only. The functions $P^+_{\nu a}$ are plotted in black on the Fig. 5f for channel flow, 6f for pipe flow, 7f for boundary layer. These figures confirm that, at fixed y/δ, P^+_ν approaches $P^+_{\nu a}$ as $Re_\tau \to \infty$.

3. Transport

Obviously

$$-\,T^+_{\nu a} \;=\; P^+_{\nu a} \;-\; D^+_{\nu a} \quad \text{or} \quad -\,T_{\nu a} \;=\; P_{\nu a} \;-\; D_{\nu a}\;, \tag{24}$$

depending on the units, yields the asymptotic profiles of the opposite of the transport term in the outer region, as proven by the Figs. 5h for channel flow, 6h for pipe flow, 7h for boundary layer.

H. Physical properties of the eddy viscosity transport profiles

From the results of the Secs. II.B to II.G, we can construct for an overview the table 1. We now focus on the profiles of the (opposite of the) transport term T_ν which is unambiguously defined, and considered as a relevant physical quantity. We can list the following physical properties of these so-called transport profiles, starting in the inner region and going progressively to the outer region.

(D0) In the inner region, in perfect agreement with the wall-damping idea, dissipation dominates: $-T_\nu \simeq -D_{\nu i}$ because $D_{\nu i}$ dominates P_ν and $D_{\nu o}$.

(D1) As $Re_\tau \to \infty$, at fixed y^+, $-T^+_\nu$ and $-D^+_{\nu i}$ converge to a universal function $-D^+_{\nu i a}(y^+)$, plotted in black on the

Table 1 The different terms in the ν_t equation, or ν_t budget, $0 = T_\nu - D_\nu + P_\nu$, at finite and infinite Re_τ , in various regions for this latter case, with analytical formulas or references to analytical formulas.

		Infinite Re_τ		
	Finite Re_τ	inner region	log layer	outer region
Dissipation	$D_\nu = D_{\nu i} + D_{\nu o}$ eq. (12a,12c)	$D_{\nu ia}(y^+) + 0$ eq. (18)	$u_\tau^2\kappa^2 + 0$	$D_{\nu a}(y/\delta)$ eq. (21)
Production	P_ν eq. (12b)	0	0	$P_{\nu a}(y/\delta)$ eq. (23)
Transport	$T_\nu = D_\nu - P_\nu$	$D_{\nu ia}(y^+)$ eq. (18)	$u_\tau^2\kappa^2$	$T_{\nu a}(y/\delta)$ eq. (24)

Fig. 5a, that peaks at $\max D^+_{\nu ia} \simeq 0.36$ around $y^+ = 31$.

(D2) For larger values of y^+, $D^+_{\nu ia} \simeq T^+_\nu$ has a minimum around $y^+ = 72$, and reaches the log-layer plateau $D^+_{\nu ia} = \kappa^2$ as soon as $y^+ \gtrsim 400$.

All this proves that dissipation of the eddy-viscosity is mainly due to universal near-wall motions.

(T0) Beyond the log-layer plateau in terms of values of y, at fixed y/δ, as $Re_\tau \to \infty$, the opposite of the transport term $-T^+_\nu$ converges to asymptotic profiles $-T^+_{\nu a}$, plotted in black on the Figs. 5h, 6h, 7h, that depend on y/δ and on the flow case only. These asymptotic profiles start at 'low' y at the log-layer plateau value $-T^+_{\nu a} = -\kappa^2$.

(P) For larger values of y, the functions $-T^+_{\nu a}$ show a maximum due to the production term around $y = 0.3\delta$.

The scaling with y/δ and the position of this maximum proves that production of the eddy-viscosity is due to large-scale outer motions.

(T1) For even larger values $y \geq 0.65\delta$, $-0.025 < -T^+_{\nu a} < 0$, i.e. dissipation dominates again, but only slightly.

The properties (D) contrast with the ones of the dissipation of the turbulent kinetic energy k, i.e., ϵ, which peaks at the wall and not off-the wall. Moreover, contrarily to D^+_ν , ϵ^+ shows no clear scaling in the near-wall region for the Reynolds numbers accessible to DNS, i.e. $Re_\tau \lesssim 6000$ in channel flow, as shown for instance by [25] and confirmed by the data of [7]; see also [26]. The properties (P) contrast strongly with the ones of the production of k, which scales with y^+ and peaks near wall, around $y^+ = 11$, as shown for instance in the supplementary material to [21]. To further illustrate these differences between the eddy-viscosity and turbulent kinetic energy budgets, the production-to-dissipation ratio of the eddy-viscosity is shown on the Figs. 8. The comparison of the Fig. 8a with the figure 7 of [7] that displays $P_k/\epsilon - 1$ (with their notations, see also our appendix A) shows huge differences. When $Re_\tau \to \infty$, whereas at fixed y^+ one has P^+_ν and $P_\nu/D_\nu \to 0$, on the contrary P_k/ϵ seems to converge to an asymptotic profile which is non-vanishing. Moreover, whereas $P_k = 0$ at the centerplane in channel flow for symmetry reasons, $P_\nu > 0$ there. The Fig. 8b shows at fixed y/δ the convergence of P_ν/D_ν to the asymptotic profile $P_{\nu a}/D_{\nu a}$. Overall, the eddy-viscosity and turbulent kinetic energy budgets differ significantly.

Regarding the ν_t production peaks, the comparison between the vertical scales of the Figs. 5f, 6f and 7f shows that the large-scale outer motions contribute more efficiently to the production of ν_t in the boundary layer than in the other flows. This shows also on the production peaks of $-T^+_\nu$, which are roughly 30% higher in the boundary layer. This is probably

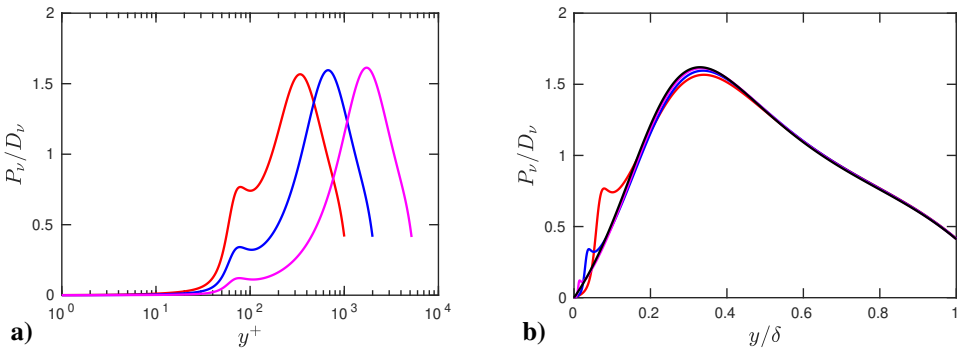

Fig. 8 Exact model for channel flows: production-to-dissipation ratio for $Re_\tau = 1000$ (red), 1995 (blue), 5186 (magenta). In (b) the black curve shows the asymptotic ratio $P_{\nu a}/D_{\nu a}$.

related to the fact that the boundary layer is in principle unbounded in the wall-normal direction, contrarily to channel and pipe flows.

The robust properties (D,T,P) of the transport profiles will now be used to study existing models of the eddy-viscosity equation.

III. Evaluation of other models and model enhancement

From now on, the focus is on channel flows, which are very well documented, and where the geometry is the most simple. Our aim is to study the performance of existing models of the eddy-viscosity equation, by a test of the properties listed in the Sec. II.H through relevant plots. Last but not least, a new version of the SAS models is proposed on this base.

A. High-Reynolds number model of Spalart & Allmaras

The high-Reynolds number eddy-viscosity equation (4) of [10] reads, for channel flow,

$$\sigma_S \frac{\partial \nu_t}{\partial t} = 0 = \frac{\partial}{\partial y}\left(\nu_t \frac{\partial \nu_t}{\partial y}\right) + c_{b2}\left(\frac{\partial \nu_t}{\partial y}\right)^2 + \sigma_S c_{b1} S \nu_t - \sigma_S c_{w1}\, f_w \left(\frac{\nu_t}{y}\right)^2 , \tag{25}$$

with the same notations, except for σ_S which stands for the σ of [10], and

$$f_w = g\left(\frac{1+c_{w3}^6}{g^6+c_{w3}^6}\right)^{1/6} , \quad g = r + c_{w2}(r^6 - r) , \quad r = \frac{\nu_t}{S\,\kappa_S^2\, y^2} , \tag{26}$$

$\sigma_S = 2/3$, $c_{b1} = 0.1355$, $c_{b2} = 0.622$, $\kappa_S = 0.41$, $c_{w1} = c_{b1}/\kappa_S + (1 + c_{b2})/\sigma_S = 2.763$, $c_{w2} = 0.3$, $c_{w3} = 2$; their von Karman constant κ_S differs slightly from ours (7). With the definitions (11) and (16) of the transport term in physical

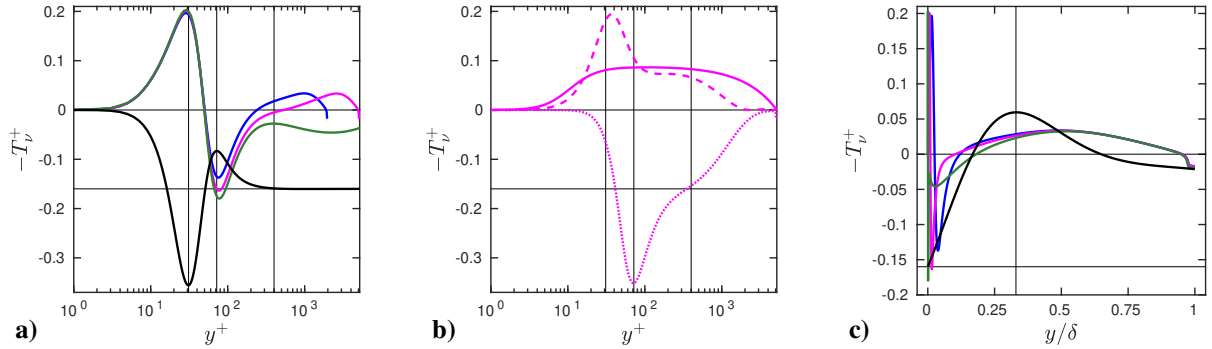

Fig. 9 Evaluation of the high-Reynolds number model of Spalart & Allmaras in channel flows. a) The black curve shows the exact $-D^+_{\nu ia}$ (18), the colored curves $-T^+_{\nu S}$ for $Re_\tau = 1995$ (blue), 5186 (magenta) and 80000 (green). b) For $Re_\tau = 5186$, the curves show $\sigma_S c_{b1} S^+ \nu^+$ (continuous), $c_{b2}\ (\partial\nu^+/\partial y^+)^2$ (dashed), $-\sigma_S c_{w1}\ f_w\ (\nu^+/y^+)^2$ (dotted). In (a,b) the vertical lines mark $y^+ = 31,\ 72$ and 400. c) The black curve shows the exact $-T^+_{\nu a}$ (24), the colored curves $-T^+_{\nu S}$ for $Re_\tau = 1995$ (blue), 5186 (magenta) and 80000 (green), the vertical line marks $y = 0.33\delta$. In (a,b,c) the horizontal lines mark $-T^+_\nu = 0$ and $-\kappa^2$.

and dimensionless forms, we identify their model for $-T^+_\nu$,

$$-T^+_{\nu S} \;=\; \sigma_S c_{b1} S^+ \nu^+ \;+\; c_{b2}\left(\frac{\partial \nu^+}{\partial y^+}\right)^2 \;-\; \sigma_S c_{w1}\, f_w \left(\frac{\nu^+}{y^+}\right)^2 \tag{27}$$

with, in particular,

$$r \;=\; \frac{\nu^+}{S^+\,\kappa_S^2\,y^{+2}}\,. \tag{28}$$

The equation (7) of [20], that takes into account wake effects, is used to compute S^+ accurately for the evaluation of the first and third terms in (27). The model (5) is used on the other hand to compute ν^+. As a first test of the model [10], plots in the inner region, with y^+ as the abscissa, are displayed on the Figs. 9ab. According to the properties (D0,D1) of the exact ν_t − equation, the colored curves of the Fig. 9a should approach, at fixed y^+, as Re_τ increases, the black curve showing $-D^+_{\nu ia}$. This is not the case, and more seriously the model [10] predicts a near-wall production peak where there should be a near-wall dissipation peak. The Fig. 9b confirms that the dissipation peak of the model occurs at too large values of y^+, and also shows that the inclusion of the production term proportional to $(\partial\nu^+/\partial y^+)^2$ does not help: it adds production where there should be more dissipation. Thus the high-Reynolds number model of [10] does not describe correctly the physics of the ν_t − equation in the near-wall region. It is also noticeable that no log-layer plateau appears in Spalart & Allmaras' model, even at $Re_\tau = 80000$, contrarily to what shows the exact ν_t − equation: compare the Figs. 5g and 9a. This raises question, since the classical 'log-layer equilibrium' has been used by [10] to relate c_{w1} to the other coefficients.

Plots with y/δ as the abscissa are displayed on the Fig. 9c. The outer production peak of $-T^+_{\nu S}$, which was already visible for the lowest values of Re_τ in the Fig. 9a, seems, on the Fig. 9c, to scale with y/δ. Moreover, the value of this outer maximum has the correct magnitude. It is also remarkable that the values of $-T^+_{\nu S}$ at $y = \delta$ are quite correct. Thus,

in the outer region there is a qualitative and even semi-quantitative agreement between the model [10] and the properties (T,P) of the exact ν_t − equation. However, the fact that the colored curves of the Fig. 9c differ significantly from the black curve, especially for the largest value of Re_τ , reveals that there are, in the outer region, quantitatively significant differences between the model and the exact theory.

In summary, the model of Spalart & Allmaras [10] appears to be of poor quality in the inner region, where it somehow inverses the production and dissipation peaks as compared to the exact model. On the contrary, it performs rather well in the outer region.

B. Model of Yoshizawa et al.

The model [12] implies three model variables: the eddy viscosity ν_t , the turbulent kinetic energy k and the turbulent dissipation ϵ. It also includes an eddy-viscosity equation, which was shown to yield a better model of ν_t than the eddy-viscosity formula of the standard $k-\epsilon$ model in some specific cases. The high-Reynolds number form of the ν_t − equation (60) of [12] reads, for channel flow,

$$\sigma_Y \frac{\partial \nu_t}{\partial t} \;=\; 0 \;=\; \frac{\partial}{\partial y}\Big(\nu_t \frac{\partial \nu_t}{\partial y}\Big) \;+\; \sigma_Y C_{\nu P}\, f_\nu\, k \;-\; \sigma_Y C_{\nu\epsilon}\, \frac{\nu_t}{\tau}\,, \tag{29}$$

with the same notations, except for σ_Y which stands for the σ_ν of [12], and

$$f_\nu \;=\; \Big(1-\exp\Big(-\frac{y^*}{14}\Big)\Big)^2 \left(1+\frac{5}{R_t^{3/4}}\exp\left(-\Big(\frac{R_t}{200}\Big)^2\right)\right), \quad \tau \;=\; \frac{k}{\epsilon\,\Lambda}\,, \quad \Lambda \;=\; \sqrt{1+2(C_S+C_\Omega)\Big(\frac{kS}{\epsilon}\Big)^2}\,, \tag{30}$$

$\sigma_Y = 3,\;\; C_{\nu P} = 4/15,\;\; C_{\nu\epsilon} = 3.5,\;\; C_S = 0.015,\; C_\Omega = 0.02 C_S,\;\; y^* = (\nu\epsilon)^{1/4}\, y/\nu,\; R_t = k^2/(\nu\epsilon)$. Their model for $-T^+_\nu$ reads therefore

$$-\,T^+_{\nu Y} \;=\; \sigma_Y C_{\nu P}\, f_\nu\, k^+ \;-\; \sigma_Y C_{\nu\epsilon}\, \frac{\epsilon^+}{k^+}\,\Lambda\,\nu^+ \tag{31}$$

with, in particular,

$$k^+ \;=\; \frac{k}{u_\tau^2}\,, \quad \epsilon^+ \;=\; \frac{\nu\epsilon}{u_\tau^4}\,, \quad y^* \;=\; (\epsilon^+)^{1/4}\, y^+\,, \quad R_t \;=\; \frac{k^{+2}}{\epsilon^+}\,, \quad \frac{kS}{\epsilon} \;=\; \frac{k^+ S^+}{\epsilon^+}\,. \tag{32}$$

Since the fields k and ϵ are needed in this model, we use the DNS data of [7] to test it. The normalized eddy viscosity ν^+ is also extracted from the DNS. Plots with y^+ as the abscissa are displayed on the Figs. 10ab. A good property of the model [12] is that it presents a dissipation peak in the near-wall region, that has the correct magnitude, and seems to scale with y^+. Thus the properties (D0,D1) of the theory are qualitatively fulfilled. However, quantitatively, the dissipation peak of $-T^+_{\nu Y}$ comes in too early in terms of y^+ values: for $Re_\tau = 5186,\;\; -\,T^+_{\nu Y}$ shows a minimum around $y^+ = 10$ instead of $y^+ = 31$ for the minimum of $-D^+_{via}$. For larger values of y^+, the model [12] appears to be too

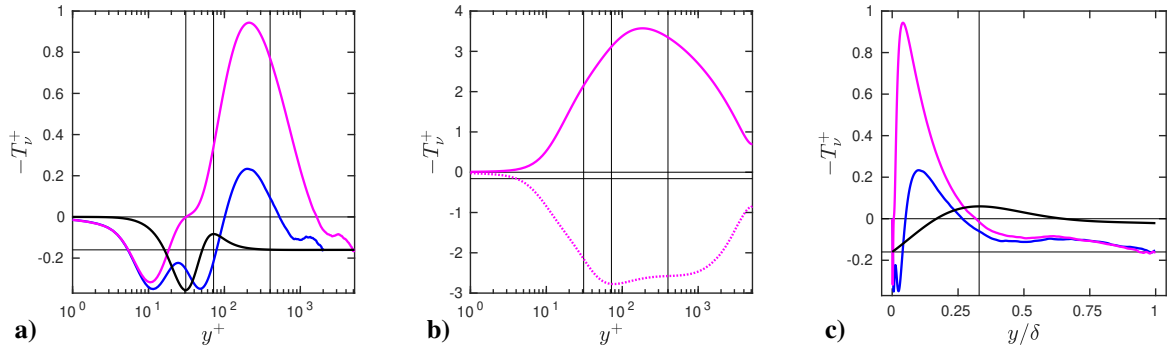

Fig. 10 Evaluation of the model of Yoshizawa et al. in channel flows, using the DNS of [7]. a) The black curve shows $-D^+_{\nu ia}$ (18), the colored curves $-T^+_{\nu Y}$ for $Re_\tau = 1995$ (blue) and 5186 (magenta). b) For $Re_\tau = 5186$, the curves show $\sigma_Y C_{\nu P}\ f_\nu\ k^+$ (continuous), $-\sigma_Y C_{\nu\epsilon}\ \frac{\epsilon^+}{k^+}\ \Lambda\ \nu^+$ (dotted). In (a,b) the vertical lines mark $y^+ = 31,\ 72$ and 400. c) The black curve shows $-T^+_{\nu a}$ (24), the colored curves $-T^+_{\nu Y}$ for $Re_\tau = 1995$ (blue) and 5186 (magenta), the vertical line marks $y = 0.33\delta$. In (a,b,c) the horizontal lines mark $-T^+_\nu = 0$ and $-\kappa^2$.

productive, and there is no log-layer plateau.

Plots with y/δ as the abscissa are displayed on the Fig. 10c. These plots confirm that the model [12] is too productive, moreover the scaling with y/δ does not show up, i.e., the properties (T,P) of the theory are not fulfilled.

In summary, the model of Yoshizawa and coworkers [12] performs rather well very close to the wall, but poorly farther away. Moreover, this model shows a too strong Reynolds-number dependence.

Importantly, the equation (60) of [12] contains a low-Reynolds number term, the viscous diffusion term

$$V_\nu \;=\; \frac{\partial}{\partial y}\Big(\nu \frac{\partial \nu_t}{\partial y}\Big)\,. \tag{33}$$

A quantitative study of this term, for channel flow, is provided in our appendix C. It is shown that, for $y^+ \geq 1$ and $Re_\tau = 1995$ or 5186, $|V^+_\nu| \leq 0.023$. This is quite smaller than the turbulent dissipation peak, $\max D^+_{\nu ia} \simeq 0.36$, which gives the order of magnitude of the transport term, see the properties (D0,D1). Thus, taking into account this term, by adding $\sigma_Y V_\nu$ to the rhs of the Eq. (29), would modify only slightly the colored curves of the Figs. 10, and the discrepancies with the exact model would not disappear.

C. SAS models of Menter et al.

1. Basic model

The high-Reynolds number $k - \sqrt{k}\ell$ SAS model of Menter et al. has been introduced in [14, 15]. The two turbulent fields are k and $\sqrt{k}\ell$ with ℓ the turbulent length scale. The product $\sqrt{k}\ell$ is up to a constant factor the eddy viscosity ν_t , hence this model can be regarded as a $k - \nu_t$ model. After multiplication by $\rho^{-1}\ c_\mu^{1/4}\ \sigma_M$, with the notations of [14],

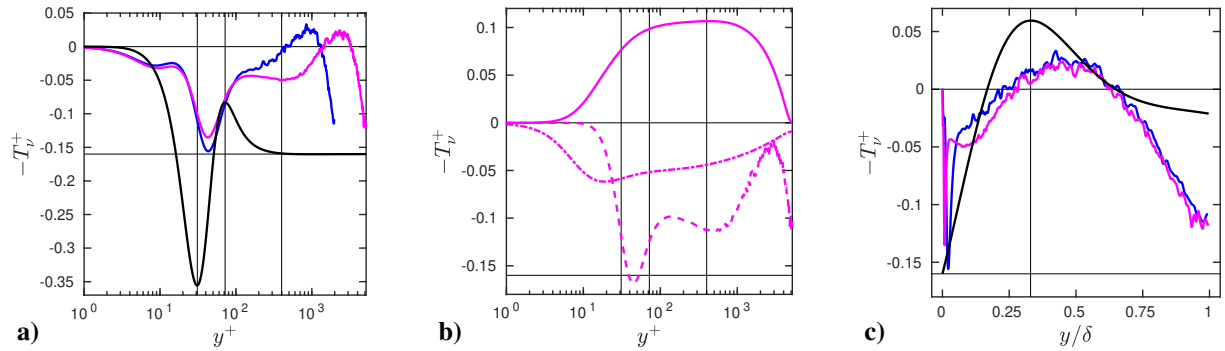

Fig. 11 Evaluation of the SAS model in channel flows, using the DNS of [7]. a) The black curve shows $-D^+_{\nu ia}$ (18), the colored curves $-T^+_{\nu M}$ for $Re_\tau = 1995$ (blue) and 5186 (magenta). b) For $Re_\tau = 5186$, the curves show $\zeta_1\ P^+_{\nu M}$ (continuous), $-\zeta_2\ P^+_{\nu M}\ (\ell/\ell_{\nu K})^2$ (dashed), $-\sigma_M c_\mu^{1/4}\zeta_3\ k^+$ (dash-dot). In (a,b) the vertical lines mark $y^+ = 31,\ 72$ and 400. c) The black curve shows $-T^+_{\nu a}$ (24), the colored curves $-T^+_{\nu M}$ for $Re_\tau = 1995$ (blue) and 5186 (magenta), the vertical line marks $y = 0.33\delta$. In (a,b,c) the horizontal lines mark $-T^+_\nu = 0$ and $-\kappa^2$.

except for σ_M which stands for their σ_Φ , their equation (7) reads, for channel flow,

$$\sigma_M \frac{\partial \nu_t}{\partial t} \ = \ 0 \ = \ \frac{\partial}{\partial y}\Big(\nu_t \frac{\partial \nu_t}{\partial y}\Big) \ + \ P_{\nu M}\left(\zeta_1 - \zeta_2\Big(\frac{\ell}{\ell_{\nu K}}\Big)^2\right) \ - \ \sigma_M c_\mu^{1/4}\zeta_3\ k \tag{34}$$

$$\text{with} \quad P_{\nu M} \ = \ \sigma_M \frac{\nu_t^2 S^2}{k}\,, \quad \ell \ = \ c_\mu^{-1/4}\ \frac{\nu_t}{\sqrt{k}}\,, \quad \ell_{\nu K} \ = \ \kappa_M \left|\frac{S}{\partial S/\partial y}\right|, \tag{35}$$

$\sigma_M = 2/3,\ c_\mu = 0.09,\ \kappa_M = 0.41,\ \zeta_1 = 0.8,\ \zeta_2 = \zeta_1 - \zeta_3/c_\mu^{3/4} + \kappa_M^2/(\sigma_M c_\mu^{1/2}) = 1.47,\ \zeta_3 = 0.0288$. The definition of the von Karman length scale in (35) agrees perfectly with our definition (14), except for the different value of the von Karman constant; for the sake of brevity we use the same notation $\ell_{\nu K}$, whereas in this section κ_M is used instead of κ for the computation of the SAS term, proportional to $(\ell/\ell_{\nu K})^2$, in (34). Menter's SAS model for $-T^+_\nu$ reads therefore

$$-\,T^+_{\nu M} \ = \ P^+_{\nu M}\left(\zeta_1 - \zeta_2\Big(\frac{\ell^+}{\ell^+_{\nu K}}\Big)^2\right) \ - \ \sigma_M c_\mu^{1/4}\zeta_3\ k^+ \tag{36}$$

$$\text{with} \quad P^+_{\nu M} \ = \ \sigma_M \frac{\nu^{+2} S^{+2}}{k^+}\,, \quad \ell^+ \ = \ c_\mu^{-1/4}\ \frac{\nu^+}{\sqrt{k^+}}\,. \tag{37}$$

The DNS data of [7] are used to test this model. Finite differences are used to compute $\partial S^+/\partial y^+$ to estimate $\ell^+_{\nu K}$. Plots with y^+ as the abscissa are displayed on the Figs. 11ab. The Fig. 11a shows that there is a near-wall dissipation peak in the SAS model, at a fixed y^+ position, i.e. the properties (D0,D1) of the theory are qualitatively fulfilled. However, the minimum value of $-T^+_{\nu M}$ corresponding to this dissipation peak is too small, and this peak comes in too late in terms of y^+ values: for $Re_\tau = 5186$, $-\,T^+_{\nu M}$ shows a minimum around $y^+ = 43$ instead of $y^+ = 31$ for the minimum of $-D^+_{\nu ia}$. For larger values of y^+, no log-layer plateau shows up in the SAS profiles, at least for $Re_\tau \lesssim 5200$, whereas the classical

'log-layer equilibrium' has been used in the derivation of the model of [14] to relate ζ_2 to the other coefficients. The Fig. 11b showing the different contributions to $-T^+_{\nu M}$ proves that the SAS term in (36) plays a quite important role, both around $y^+ = 43$ where $-T^+_{\nu M}$ has a negative peak, and near the centerplane, at $y^+ = \delta^+$, where it imposes a rather large negative value.

Plots with y/δ as the abscissa are displayed on the Fig. 11c. They show that $-T^+_{\nu M}$ scales with y/δ in the outer region, with a production peak around $y = 0.42\delta$, and then a decrease towards a negative value at the centerplane. Thus the properties (T,P) of the theory are qualitatively fulfilled.

In summary, out of the three models tested up to now, the basic SAS model shows the best qualitative and semi-quantitative agreement with the theory.

2. Study of the length scales and of the model with length scale limiters

In order to better analyze the SAS models, the Figs. 12abc display the two length scales implied and their ratio. The Figs. 12ab suggest that both length scales, scaled by δ, scale with y/δ, except in a narrow near-wall region for $\ell_{\nu K}$. Since $\ell_{\nu K}/\delta$ is computed from the DNS as

$$\frac{\ell^+_{\nu K}}{\delta^+} \;=\; \frac{\kappa_M}{\delta^+}\left|\frac{S^+}{\partial S^+/\partial y^+}\right|, \tag{38}$$

because both S^+ and $\partial S^+/\partial y^+$ become quite small in the outer region for large Re_τ , the DNS noise is amplified there. This explains the oscillations in the Figs. 12bc, that also blur some profiles in the Figs. 11. Smoother profiles of $\ell_{\nu K}$ may be obtained from the exact model of [20, 21] and have been shown on the Figs. 2. The laws that result from the log-layer theory,

$$\ell \;=\; \ell_{\nu K} \;=\; \kappa_M y\,, \tag{39}$$

are relevant in a narrow near-wall region for ℓ and in a larger region for $\ell_{\nu K}$, which otherwise vanishes at the centerplane as already discussed after Eq. (14). The ratio $\ell/\ell_{\nu K}$ displayed on the Fig. 12c shows consequently a near-wall peak of maximum value of order 1, which locates somehow the log-layer region. It then decays, since $\ell_{\nu K}$ increases first faster than ℓ, and finally increases again and diverges as $y \to \delta$. Obviously, the infinite value of $\ell/\ell_{\nu K}$ at the centerplane plays a role in the too large value of $-T^+_{\nu M}$ in this region, see the Figs. 11bc.

From these observations, it seems relevant to test also the SAS model with length scale limiters, since these limiters have been defined 'in order of avoiding overly large or small values of the length scale ratio' $\ell/\ell_{\nu K}$, as explained by [14] at the level of their equation (12). These length scale limiters are defined by

$$\ell/c_{\ell 1} \;<\; \ell_{\nu K} \;<\; c_{\ell 2}\,\kappa_M\, y \tag{40}$$

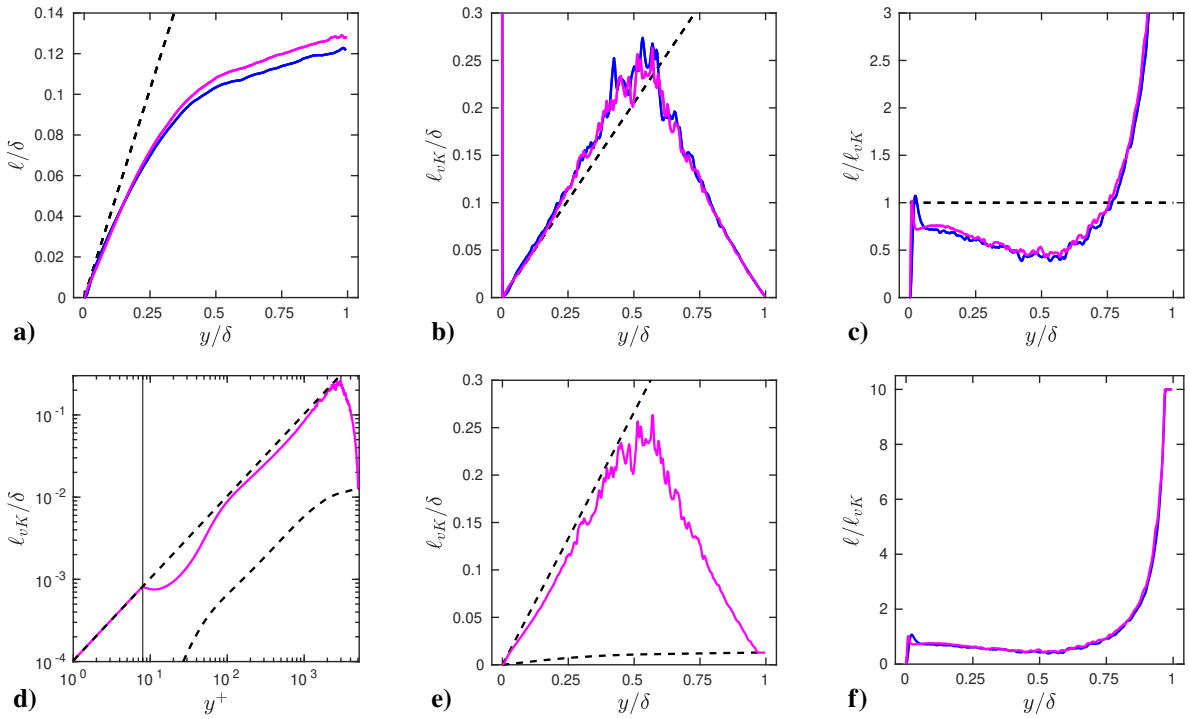

Fig. 12 Length scales of the SAS model in channel flows, using the DNS of [7] at $Re_\tau = 1995$ (blue) and 5186 (magenta): a) the turbulent length scale ℓ, b) the von Karman length scale ℓ_{vK} , c) their ratio. In (a,b) the dashed line shows the log-layer length scale $\kappa_M y^+$. The effects of the length scale limiters (40) is shown on (d,e) for $Re_\tau = 5186$, with the limiters shown by the dashed curves, and on (f) for both Reynolds numbers.

with $c_{\ell 1} = 10,\ c_{\ell 2} = 1.3$. These limiters are displayed on the Figs. 12de for the highest Reynolds number available in the DNS of [7]. The maximum limiter is active in a narrow near-wall region, for $y^+ \lesssim 8$. There ℓ is quite small, hence ℓ/ℓ_{vK} remains small and is unchanged at the scales of the Figs. 12cf. The minimum limiter is active in a narrow region near the centerplane. As displayed on the Fig. 12f, the length scale ratio is mainly affected in this outer region, where it saturates to $\ell/\ell_{vK} = c_{\ell 1}$. This saturates the minimum peak of $-T^+_{\nu M}$ at the centerplane only marginaly, with reference to the Figs. 11bc. From this point of view, a lower value of $c_{\ell 1}$ would help.

3. Model with a viscous sublayer term

In order to have a model valid through the viscous sublayer, [14] add a viscous sublayer term to the r.h.s. of their ν_t - Eq. (34),

$$VSM_\nu \ = \ -6\sigma_M \ f_\Phi \ \frac{\nu\nu_t}{y^2} \ . \tag{41}$$

The dimensional factor in this term, $\nu\nu_t/y^2$, has similarities with the one of the last term of the ν_t - Eq. (25) of [10], ν_t^2/y^2, with, however, one eddy viscosity replaced by the fluid viscosity. In (41),

$$f_\Phi \ = \ \frac{1 + c_{d1}\xi}{1 + \xi^4} \ , \quad \xi \ = \ \frac{\sqrt{0.3\ k}\ y}{20\nu} \ , \quad c_{d1} = 4.7 \ . \tag{42}$$

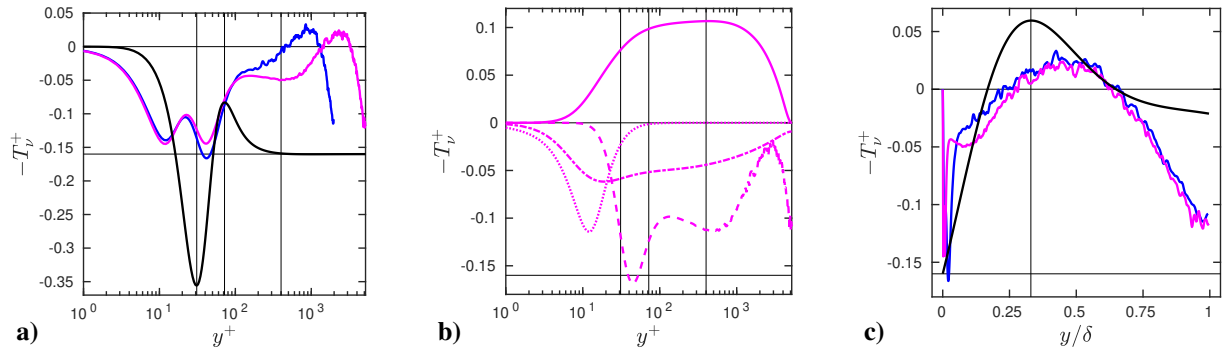

Fig. 13 Same as Figs. 11, but adding the viscous sublayer term VSM_ν^+ (43) to $-T_{\nu M}^+$ (36); VSM_ν^+ is shown with the dotted curve in (b).

In inner units,

$$VSM_\nu^+ \;=\; -\,6\sigma_M\, f_\Phi\, \frac{\nu^+}{y^{+2}} \quad \text{with} \quad \xi \;=\; \frac{\sqrt{0.3\,k^+}\,y^+}{20} \tag{43}$$

in the damping function f_Φ . The Figs. 13 show that the addition of VSM_ν^+ to $-T_{\nu M}^+$ introduce a new near-wall minimum peak in $-T_{\nu M}^+$, which does not really help since it occurs at too low values of y^+, and is too weak.

4. Model with ν_t limiter

For the sake of completeness, we check that the ν_t limiter introduced in [14] to deal with adverse pressure gradients or stagnation regions is inactive in channel flow. The equations (11) of [14] state that the normalized eddy viscosity ν^+ should be smaller than

$$\nu_m^+ \;=\; \frac{a_1 k^+}{S^+} \quad \text{with} \quad a_1 = a_1^{SST} f_b + (1-f_b) a_1^{REAL}\,, \quad f_b = \tanh\left[\left(\frac{20(\nu^+ + 1)}{\kappa_M S^+ y^{+2} + 0.01}\right)^2\right], \tag{44}$$

$a_1^{SST} = 0.32,\ a_1^{REAL} = 0.577$. Because the turbulent kinetic energy k^+ reaches rather large levels in the near-wall region, and then does not decrease too much outside, as shown on the Fig. 14a, whereas the mean strain rate S^+ decreases fast from 1 to 0 as y increases from 0 to δ, ν_m^+ is everywhere larger than ν^+, as shown on the Figs. 14bc.

D. New SAS model

In channel flow, as discussed in the Sec. III.C.1 and displayed in the Fig. 11a, the main problem with the SAS model is that the dissipation-related peak in the near-wall region is too weak and occurs too late. Another secondary problem, displayed in the Fig. 11c, is that the SAS model is on the contrary too dissipative in the centerplane region. Because the Fig. 11b shows that the SAS dissipation term

$$D_{\nu M} \;=\; \zeta_2 P_{\nu M} \left(\frac{\ell}{\ell_{\nu K}}\right)^2 \;=\; \zeta_2 \sigma_M \frac{\nu_t^2 S^2}{k} \left(\frac{\ell}{\ell_{\nu K}}\right)^2 \tag{45}$$

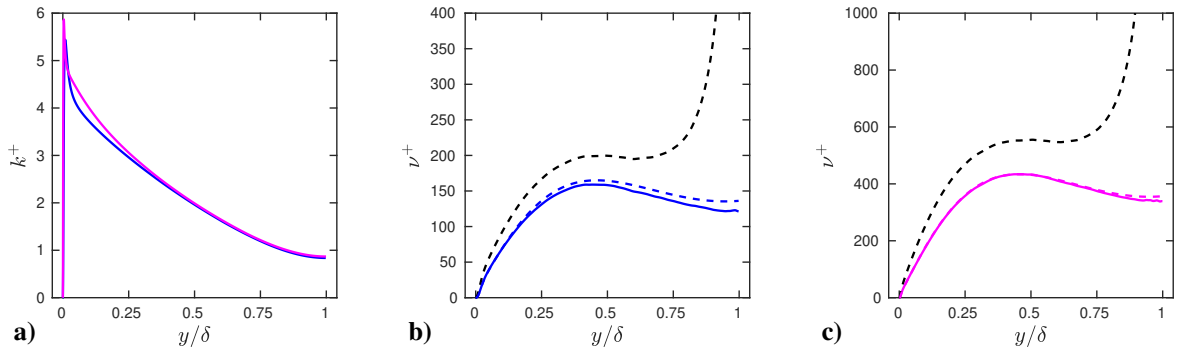

Fig. 14 Various fields in channel flows. a) The turbulent kinetic energy k^+ for the DNS of [7] at $Re_\tau = 1995$ (blue) and 5186 (magenta). b,c) For $Re_\tau = 1995$ (b) or 5186 (c) the continuous colored curve shows ν^+ computed from the DNS, the continuous dashed curve ν^+ (5), the black dashed curve ν_m^+ (44).

of Eq. (34) dominates in the near-wall and centerplane regions, it is worthwhile to test a modified SAS model where the terms proportional to ζ_1 and ζ_3 in Eq. (34) are kept, whereas $D_{\nu M}$ is replaced by a term similar to the exact $D_{\nu i}$ (12a),

$$D_{\nu N} \;=\; \kappa^2\,\frac{\nu_t^2}{\ell_{\nu K}^2}\,\frac{1}{f^2}\;. \tag{46}$$

The replacement of $L_{\nu K}$ in $D_{\nu i}$ by $\ell_{\nu K}$ in $D_{\nu N}$ is important to ensure that this modified model may be as 'sensitive' as the original SAS model: both the original and modified dissipation terms are proportional to $\ell_{\nu K}^{-2}$. Our modified SAS ν_t - equation thus reads, in turbulent wall flows,

$$\sigma_M\frac{\partial \nu_t}{\partial t} \;=\; 0 \;=\; \frac{\partial}{\partial y}\Big(\nu_t\frac{\partial \nu_t}{\partial y}\Big) \;+\; \zeta_1 P_{\nu M} \;-\; D_{\nu N} \;-\; \sigma_M c_\mu^{1/4}\zeta_3\; k\;. \tag{47}$$

To obtain a correct behaviour of $D_{\nu N}$ in the near-wall region, that is, a behaviour similar to that of $D_{\nu i}$, it is important to not use a maximum limiter of $\ell_{\nu K}$ proportional to y, as Menter et al. did it, see (40) and the Fig. 12d. This would impose $\ell_{\nu K} = 0$ at the wall, which is probably not very physical, and would surely break the subbtle balance between ν_t and $L_{\nu K} f$ in $D_{\nu i}$ or $\ell_{\nu K} f$ in $D_{\nu N}$ that insures that these dissipation terms behave smoothly as $y \to 0$. Therefore, we use only a minimum limiter on $\ell_{\nu K}$,

$$\ell/c_{\ell 1} \;<\; \ell_{\nu K}\;, \tag{48}$$

with a lower value of $c_{\ell 1} = 1$ to saturate $D_{\nu N}$ near the centerplane. With the same coefficients ζ_1 , ζ_3 as the ones chosen by Menter et al., a test of this new model, which leads to

$$-\,T_{\nu N}^+ \;=\; \zeta_1 P_{\nu M}^+ \;-\; D_{\nu N}^+ \;-\; \sigma_M c_\mu^{1/4}\zeta_3\; k^+ \tag{49}$$

$$\text{with}\quad D_{\nu N}^+ \;=\; \kappa^2\,\frac{\nu^{+2}}{\ell_{\nu K}^{+2}}\,\frac{1}{f^2}\;, \tag{50}$$

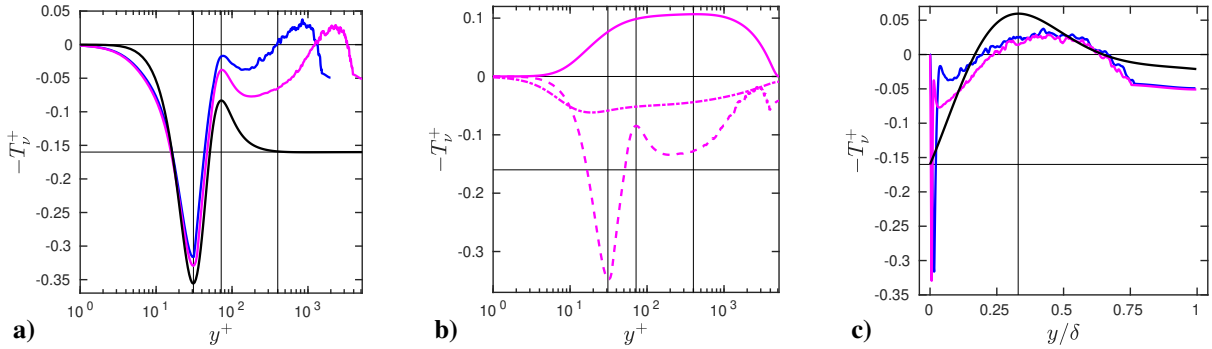

Fig. 15 Evaluation of the new SAS model (47) in channel flow, using the DNS of [7]. a) The black curve shows $-D^+_{\nu ia}$ (18), the colored curves $-T^+_{\nu N}$ (49) for $Re_\tau = 1995$ (blue) and 5186 (magenta). b) For $Re_\tau = 5186$, the curves show $\zeta_1\ P^+_{\nu M}$ (continuous), $-D^+_{\nu N}$ (dashed), $-\sigma_M c_\mu^{1/4}\zeta_3\ k^+$ (dash-dot). In (a,b) the vertical lines mark $y^+ = 31,\ 72$ and 400. c) The black curve shows $-T^+_{\nu a}$ (24), the colored curves $-T^+_{\nu M}$ for $Re_\tau = 1995$ (blue) and 5186 (magenta), the vertical line marks $y = 0.33\delta$. In (a,b,c) the horizontal lines mark $-T^+_\nu = 0$ and $-\kappa^2$.

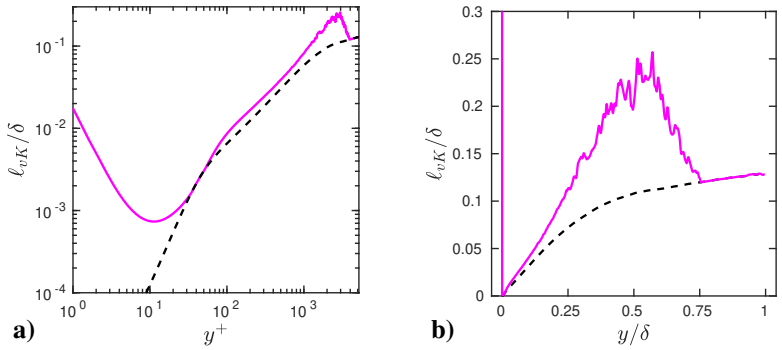

Fig. 16 Length scales of the new SAS model (47) in channel flow, using the DNS of [7] at $Re_\tau = 5186$: the magenta curves show the limited von Karman length scale $\ell_{\nu K}$ and the black curves its limiter, the turbulent length scale ℓ.

is shown in Figs. 15. The comparison with the Figs. 11 proves that a much better agreement with the exact model is reached. More precisely, the curves of the Fig. 15a are quite similar to the corresponding ones of the Fig. 5g, whereas the ones of the Fig. 15c are very similar to the corresponding ones of the Fig. 5h: now all the properties (D,T,P) of the exact model, listed in the Sec. II.H, are quantitatively recovered.

To complete the presentation of this new model, the von Karman length scale and its minimum limiter, i.e., the turbulent length scale, are plotted on the Figs. 16, which should be compared to the Figs. 12de. Note that $\kappa = 0.40$ has been used in this section, instead of $\kappa_M = 0.41$ in the previous one.

IV. Summary and discussion

The recent availability of the extended DNS and experimental databases of [7] for channel flows, [22] for pipe flows, [23, 24] for boundary layers, that span wide intervals of values of Reynolds numbers, has allowed the development of the analytic RANS theory of [20, 21] for these turbulent wall flows. This theory offers the analytic formula (5) for the

eddy viscosity ν_t , which is remarkably shear driven: the mean shear S (2) plays a central role, and, on the contrary, the turbulent kinetic energy does not intervene. This theory has been used here to derive an exact transport Eq. (10) for ν_t that contains a standard transport term T_ν balanced by production and dissipation terms, P_ν and D_ν , in steady mean flows: for such flows the equation reads simply $T_\nu + P_\nu - D_\nu = 0$. It is 'exact' in that all the terms are known analytically, as functions of the inner shear function S_{12}^+ and wake functions W determined from [20, 21], at finite and infinite Re_τ , either in the inner, log layer or outer regions for the latter case, as summarized on the table 1.

To our knowledge, this is the first time that an exact scale-determining equation has been determined for a RANS model, and analyzed in details: the eddy viscosity budget is fully determined at finite and infinite Reynolds numbers. All this offers a vision of the mechanisms at play, as summarized in our Sec. II.H, which also shows that our ν_t budget and the known k budget (at finite Reynolds number only) differ quite much. In the ν_t budget, noticeable is the existence of a universal near-wall dissipation peak (Figs. 5g, 6g, 7g), in perfect agreement with the wall-damping idea. Indeed, the dissipation takes the same universal form $D_{\nu i}$ (12a) for all turbulent wall flows. This form identifies as the relevant length scale the universal asymptotic von Karman length scale $L_{\nu K}$ (13) and a universal damping function f (15).

All this has been used as a physical test bench of existing models that present a ν_t equation with the same transport term T_ν . Thus, we have evidenced some deficiencies of the high Reynolds number models of Spalart & Allmaras [10], Yoshizawa *et al.* [12], which were designed before the publication of the databases mentioned [7, 22–24]: both models display a strong ν_t production peak in the near-wall region (Figs. 9 and 10). In other words, the physics of their ν_t budget is incorrect in this region. Since wall-flows are basically driven by the wall effect, the unphysical treatment of the near-wall region in these models has to be expected to imply unphysical turbulence simulations. Regarding the model of Spalart & Allmaras [10], we studied only the high Reynolds number, baseline form of their ν_t equation (their equation 4), whereas their final equation (9), that should work in principle at finite Reynolds number, implies a modified eddy-viscosity $\widetilde{\nu}$ given by a highly nonlinear function of ν_t , as defined in their equation (7). We show however in our appendix D that this change of variable does not resolve the 'wall-damping problem', i.e., in the near-wall region, strong discrepancies between the exact model and the final model of Spalart & Allmaras remain.

The SAS models of [14, 15] have also been studied, in steady RANS mode, and have given better results. Quantitative discrepancies between the SAS ν_t budget and our exact ν_t budget, i.e., too weak near-wall dissipation peaks, plus over-dissipation in the outer region, have been resolved by a modification of the SAS dissipation term in the ν_t equation. We suggest to use the form of the exact $D_{\nu i}$ (12a), but replacing the universal asymptotic von Karman length scale $L_{\nu K}$ by the local von Karman length scale $\ell_{\nu K}$ (14), limited from below by the turbulent length scale ℓ. This limited von Karman length scale shows, at least in channel flow, a profile rather similar to the one of $L_{\nu K}$: compare the Figs. 2ab and 16ab. This yields a much better match with the exact model, both in the inner and outer regions: compare finally the Figs. 11, 13 and 15. The fact that the limited von Karman length scale is flow-dependent and appears at the power -2 in the dissipation term suggests that the new model could be, in unsteady simulations of complex flows, as 'instability

sensitive' or 'scale-adaptive' as the models of [14, 15]. The main advantage of our model presented here is the correct capture of the near-wall dissipation peak. To avoid the use of the scaled wall-normal distance y^+ in the function f of the new dissipation term (46), it may be good to use ideas of the elliptic relaxation methods [27].

Appendix A: Validation of the standard k equation with channel flow DNS

In the standard, high-Reynolds number $k-\omega$ [5] and $k-\epsilon$ [6] models, for channel flows, the closed k equation reads

$$\sigma_k \frac{\partial k}{\partial t} \;=\; 0 \;=\; \frac{\partial}{\partial y}\Big(\nu_t \;\frac{\partial k}{\partial y}\Big) \;+\; \sigma_k \;(P_k \;-\; \epsilon) \tag{51}$$

with σ_k a model coefficient, and the production term

$$P_k \;=\; \nu_t \; S^2$$

according to the eddy-viscosity hypothesis, with the notations of Sec. II.A. The Eq. (51) is also used in the SAS model of [14, 15]. Various values of σ_k are recommended: $\sigma_k = 2$ in [5], 1 in [6], $2/3$ in [14]. To discriminate between those, and confirm the relevance of the k - equation, we analyze the Eq. (51) with the approach of [28]. After division by ϵ, Eq. (51) states that the opposite of the dimensionless normalized transport term

$$-\,T'_k \;=\; -\,\frac{1}{\epsilon}\frac{\partial}{\partial y}\Big(\nu_t \;\frac{\partial k}{\partial y}\Big) \tag{52}$$

should be a linear function of the production-to-dissipation ratio P_k/ϵ,

$$-\,T'_k \;=\; \sigma_k \;(P_k/\epsilon \;-\; 1)\;. \tag{53}$$

This prediction is tested on the channel flow DNS data of [7] on the Figs. A1. Note that [7] offer in their figure 7 plots of P_k/ϵ vs y^+. The eddy viscosity ν_t is computed according to its definition (3), and the derivatives by y in T'_k are computed by finite differences. The Figs. A1 show that, in the outer region $y^+ > 15$, the DNS curves remain close to the line (53): this confirms the relevance of the high-Reynolds number k - Eq. (51), and supports [14] in their choice $\sigma_k = 2/3$. The value of [6], $\sigma_k = 1$, seems a bit too large, whereas the value of [5], $\sigma_k = 2$, seems clearly too large.

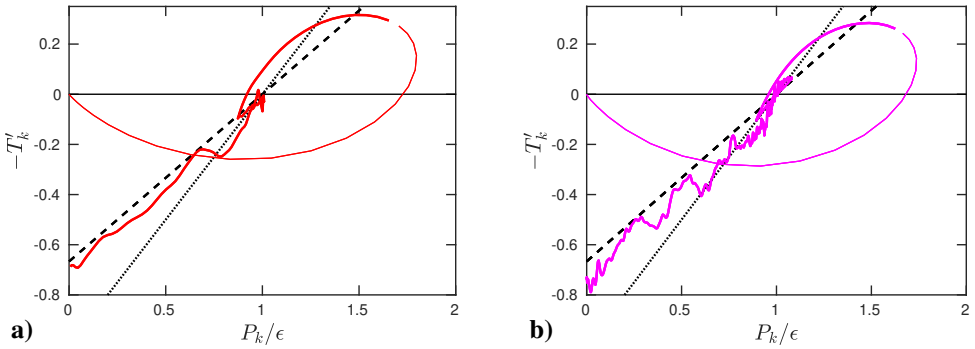

Fig. A1 Test of the k equation of the $k-\epsilon$ model in channel flows. The continuous curve shows the opposite of the normalized transport term $-T_k'$ vs the ratio P_k/ϵ for the DNS of [7] at $Re_\tau = 543$ (a), 5186 (b). The thin (resp. thick) curve corresponds to the inner region $y^+ < 15$ (resp. outer region $y^+ > 15$). The dashed (resp. dotted) line shows the model $\sigma_k\ (P_k/\epsilon\ -\ 1)$ with $\sigma_k = 2/3$ (resp. 1).

Appendix B: Study of the standard ϵ and ω equations with channel flow DNS

By analogy with (51), [6] postulated in the $k-\epsilon$ model the ϵ equation, for channel flows,

$$\sigma_\epsilon \frac{\partial \epsilon}{\partial t} \;=\; 0 \;=\; \frac{\partial}{\partial y}\Big(\nu_t\, \frac{\partial \epsilon}{\partial y}\Big) \;+\; \sigma_\epsilon \frac{\epsilon}{k}\,(C_1 P_k \;-\; C_2 \epsilon) \tag{54}$$

with $\sigma_\epsilon = 1.3,\ C_1 = 1.44,\ C_2 = 1.92$. After division by ϵ^2/k, Eq. (54) states that the opposite of the normalized transport term

$$-\,T_\epsilon' \;=\; -\,\frac{k}{\epsilon^2}\frac{\partial}{\partial y}\Big(\nu_t\, \frac{\partial \epsilon}{\partial y}\Big) \tag{55}$$

should be a linear function of P_k/ϵ,

$$-\,T_\epsilon' \;=\; \sigma_\epsilon\ (C_1 P_k/\epsilon \;-\; C_2)\ . \tag{56}$$

This prediction is tested on the channel flow DNS of [7] on the Figs. B1. Since ϵ becomes quite small near the centerplane (see e.g. the figure 9 of [21]), there the DNS noise is amplified: this region corresponds to the lower intersection of the curves of the Figs. B1 with the axis $P_k/\epsilon = 0$ i.e. $P_k = 0$ (see the figure 7 of [7]). The Figs. B1, to be compared with the Figs. A1, show DNS curves that do not align with the linear model (56), even if one considers only their outer-region part. The structure of the curves is highly nonlinear, therefore a change of the model constants σ_ϵ , C_1 and C_2 cannot solve this problem.

A similar flaw exists with the ω equation of the standard $k-\omega$ model of [5]. With a slight change of notation, to introduce a coefficient σ_ω that plays a role similar to the coefficients σ_k in (51) and σ_ϵ in (54), Wilcox' equation for

$$\omega \;=\; \epsilon/(\beta^* k)$$

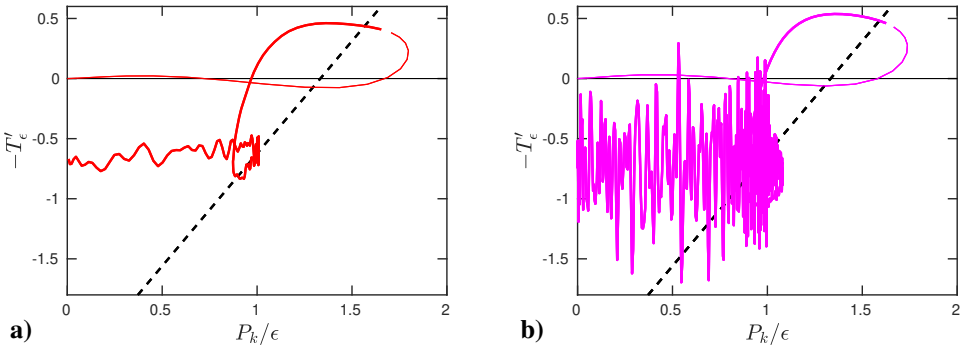

Fig. B1 Test of the ϵ equation of the $k-\epsilon$ model in channel flows. The continuous curve shows the opposite of the normalized transport term $-T'_\epsilon$ for the DNS of [7] at $Re_\tau = 543$ (a), 5186 (b). The thin (resp. thick) curve corresponds to the inner region $y^+ < 15$ (resp. outer region $y^+ > 15$). The dashed line shows the standard model $\sigma_\epsilon\ (C_1 P_k/\epsilon\ -\ C_2)$.

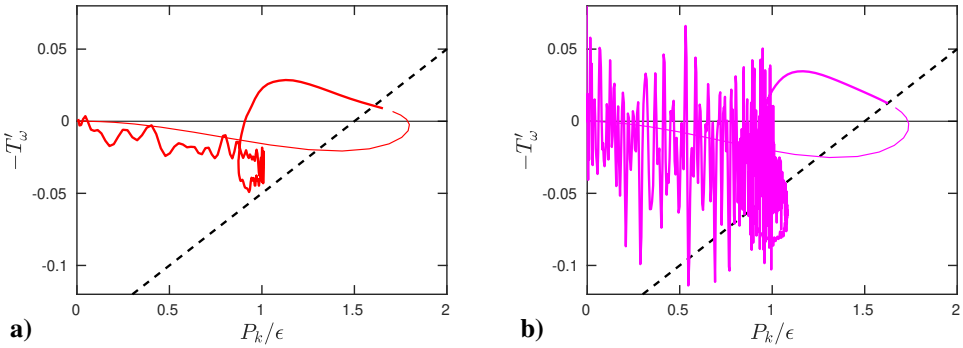

Fig. B2 Test of the ω equation of the $k-\omega$ model in channel flows. The continuous curve shows the opposite of the normalized transport term $-T'_\omega$ for the DNS of [7] at $Re_\tau = 543$ (a), 5186 (b). The thin (resp. thick) curve corresponds to the inner region $y^+ < 15$ (resp. outer region $y^+ > 15$). The dashed line shows the standard model $\sigma_\omega\ (\beta^* \gamma P_k/\epsilon\ -\ \beta)$.

reads, for channel flows,

$$\sigma_\omega \frac{\partial \omega}{\partial t} \;=\; 0 \;=\; \frac{\partial}{\partial y}\left(\nu_t\ \frac{\partial \omega}{\partial y}\right) \;+\; \sigma_\omega \frac{\omega}{k}\left(\gamma P_k \;-\; \frac{\beta}{\beta^*}\epsilon\right) \tag{57}$$

where $\sigma_\omega = 2,\ \gamma = 5/9,\ \beta = 3/40,\ \beta^* = 9/100$. After division by ω^2, Eq. (57) states that

$$-\,T'_\omega \;=\; -\,\frac{1}{\omega^2}\frac{\partial}{\partial y}\left(\nu_t\ \frac{\partial \omega}{\partial y}\right) \tag{58}$$

should be a linear function of P_k/ϵ,

$$-\,T'_\omega \;=\; \sigma_\omega\ (\beta^* \gamma P_k/\epsilon\ -\ \beta)\ . \tag{59}$$

The Figs. B2 show again a highly nonlinear structure of the channel flow DNS curves, that cannot fit a linear model such as (59), even in the outer region $y^+ > 15$.

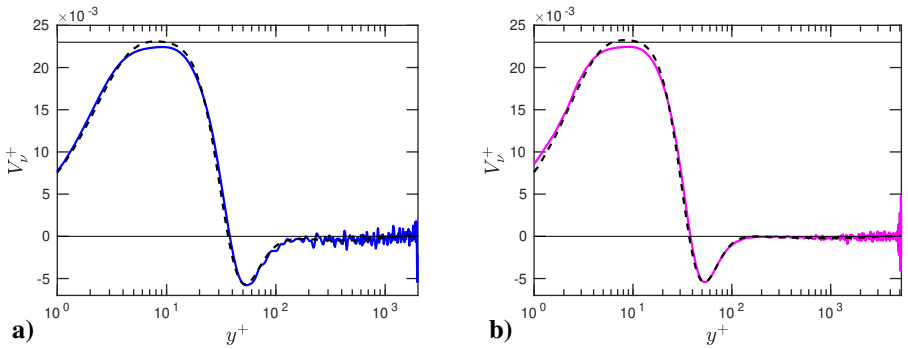

Fig. C1 Viscous diffusion term in the ν_t equation for channel flows. The continuous curve is computed with the DNS of [7] at $Re_\tau = 1995$ (a), 5186 (b). The dashed curve shows the analytical model that can be derived from (5). The horizontal lines mark $V_\nu^+ = 0$ and 0.023.

Appendix C: Viscous diffusion term in the ν_t equation

The viscous diffusion term V_ν defined in the Eq. (33) reads, in dimensionless form,

$$V_\nu^+ = \frac{V_\nu}{u_\tau^2} = \frac{\partial^2 \nu^+}{\partial y^{+2}} . \tag{60}$$

It can be computed numerically with finite differences from channel flow DNS data. It can also be computed analytically starting from (5). A comparison of both estimates of V_ν^+, for relevant cases (the ones also studied in Sec. III.B), is displayed on the Figs. C1. The analytic model is overall quite good. Moreover, everywhere, $|V_\nu^+| \leq 0.023$.

Appendix D: Evaluation of the finite Reynolds number model of Spalart & Allmaras

For finite Reynolds number, [10] propose to use, instead of the eddy viscosity ν_t , an undamped eddy-viscosity $\widetilde{\nu}$ defined by

$$\nu_t = \widetilde{\nu}\, f_{v1} = \nu\chi\, f_{v1} \quad \text{with} \quad f_{v1} = \frac{\chi^3}{\chi^3 + c_{v1}^3} \quad \text{and} \quad c_{v1} = 7.1 . \tag{61}$$

This eddy-viscosity $\widetilde{\nu}$ is undamped because it is much larger than ν_t in the near-wall region. For channel flow, $\widetilde{\nu}$ fulfills the transport equation

$$\sigma_S \frac{\partial \widetilde{\nu}}{\partial t} = 0 = \frac{\partial}{\partial y}\left(\nu \frac{\partial \widetilde{\nu}}{\partial y}\right) + \frac{\partial}{\partial y}\left(\widetilde{\nu} \frac{\partial \widetilde{\nu}}{\partial y}\right) + c_{b2}\left(\frac{\partial \widetilde{\nu}}{\partial y}\right)^2 + \sigma_S c_{b1} \widetilde{S} \widetilde{\nu} - \sigma_S c_{w1}\, f_w \left(\frac{\widetilde{\nu}}{y}\right)^2 . \tag{62}$$

There a modified mean strain rate $\widetilde{S}$ enters,

$$\widetilde{S} = S + \frac{\widetilde{\nu}}{\kappa_S^2 y^2} f_{v2} \quad \text{with} \quad f_{v2} = 1 - \frac{\chi}{1 + \chi f_{v1}} , \tag{63}$$

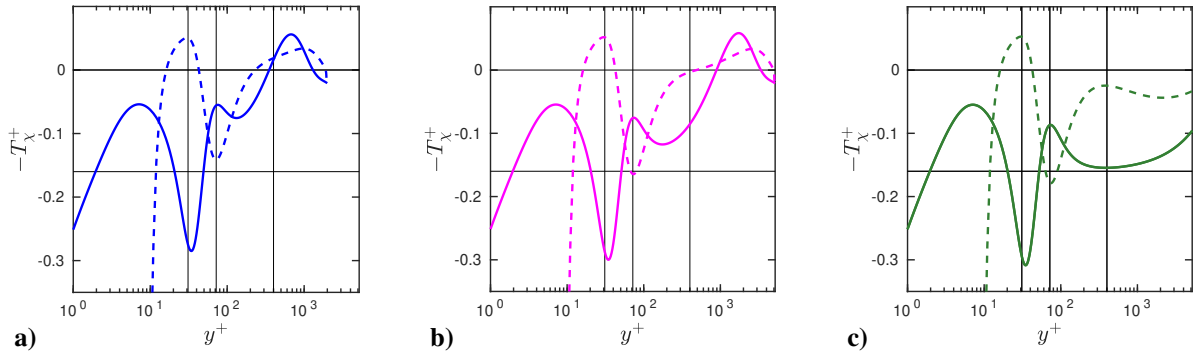

Fig. D1 Evaluation of the finite Reynolds number model of Spalart & Allmaras in channel flow for $Re_\tau = 1995$ (a), 5186 (b), 80000 (c). The continuous colored lines show the exact $-T_\chi^+$, the dashed colored lines their model $T_{\chi S}^+$. The black lines are the same as in Fig. 9a.

and it is also important to change the variable r in the definition (26) of f_w ,

$$r \;=\; \frac{\widetilde{\nu}}{\widetilde{S}\,\kappa_S^2\,y^2}\,. \tag{64}$$

With inner units, the transport Eq. (62) takes the dimensionless form

$$0 \;=\; \frac{\partial^2\chi}{\partial y^{+2}} \;+\; \frac{\partial}{\partial y^+}\Big(\chi\,\frac{\partial\chi}{\partial y^+}\Big) \;+\; c_{b2}\Big(\frac{\partial\chi}{\partial y^+}\Big)^2 \;+\; \sigma_S c_{b1}\widetilde{S}^+\chi \;-\; \sigma_S c_{w1}\,f_w\,\Big(\frac{\chi}{y^+}\Big)^2\,, \tag{65}$$

where, in particular,

$$\widetilde{S}^+ \;=\; S^+ \;+\; \frac{\chi}{\kappa_S^2 y^{+2}}\,f_{v2}\,, \quad r \;=\; \frac{\chi}{\widetilde{S}^+\kappa_S^2 y^{+2}}\,. \tag{66}$$

We checked that the first term on the r.h.s. of the Eq. (65), which is a viscous diffusion term, is negligible in front of the sum of the other terms. Neglecting this term, the transport Eq. (65) for the dimensionless undamped eddy-viscosity χ reads

$$-\,T_\chi^+ \;=\; -\,\frac{\partial}{\partial y^+}\Big(\chi\,\frac{\partial\chi}{\partial y^+}\Big) \;=\; -\,T_{\chi S}^+ \;=\; \sigma_S c_{b1}\widetilde{S}^+\chi \;+\; c_{b2}\Big(\frac{\partial\chi}{\partial y^+}\Big)^2 \;-\; \sigma_S c_{w1}\,f_w\,\Big(\frac{\chi}{y^+}\Big)^2\,. \tag{67}$$

With formal computations, χ and T_χ^+ can be obtained from our exact model (5). A comparison with the Spalart - Allmaras' model $T_{\chi S}^+$ given by the rightmost sum in (67), which is somehow a new version of the model presented in our Eq. (27), is then possible. The Figs. D1 thus obtained shows exact profiles that are similar, as soon as $y^+ \gtrsim 40$, to those displayed on the Fig. 5g. Indeed, when $y^+ \to \infty$, $\chi \sim \nu^+$ hence $T_\chi^+ \sim T_\nu^+$. Because χ is undamped, it is singular as $y^+ \to 0$, hence at the wall $T_\chi^+ \to -\infty$. For $y^+ < 10$, the Figs. D1 show that T_χ^+ and $T_{\chi S}^+$ differ much, which is a first indication that the Spalart & Allmaras model has some flaws. The situation in the vicinity of the dissipation peak of the exact transport profile, around $y^+ = 34$, is somehow worse, since there the Spalart & Allmaras model displays a

production peak. This is in line with the behaviour already displayed, with the high-Reynolds number model, in our Fig. 9a.

Acknowledgments

EP thanks J. Peinke for invitations at ForWind (Oldenburg, Germany), during which he met SH. SH acknowledges support from the National Science Foundation (DMS - CDS&E-MSS, Grant 1622488, with Dr. Y. Zeng as the Technical Officer), and from the Hanse-Wissenschaftskolleg (Delmenhorst, Germany, with W. Stenzel as the Technical Officer).

References

[1] Wilcox, D. C., *Turbulence Modeling for CFD*, DCW Industries, 2006.

[2] Hanjalić, K., and Launder, B., *Modelling turbulence in engineering and the environment: second-moment routes to closure*, Cambridge University Press, 2011.

[3] Heinz, S., "A review of hybrid RANS-LES methods for turbulent flows: Concepts and applications," *Progress in Aerospace Sciences*, Vol. 114, 2020, p. 100597.

[4] Kolmogorov, A. N., "Equations of turbulent motion in an incompressible fluid," *Selected works of A. N. Kolmogorov*, Springer 1991, 1942, pp. 328–330. Ed. V. M. Tikhomirov, translated from the Russian by V. M. Volosov.

[5] Wilcox, D. C., "Reassessment of the scale-determining equation for advanced turbulence models," *AIAA Journal*, Vol. 26, 1988, pp. 1299–1310.

[6] Launder, B. E., and Spalding, D. B., "The numerical computation of turbulent flows," *Computer Methods in Applied Mechanics and Engineering*, Vol. 3, 1974, pp. 269–289.

[7] Lee, M., and Moser, R. D., "Direct numerical simulation of turbulent channel flow up to $Re_\tau \approx 5200$," *Journal of Fluid Mechanics*, Vol. 774, 2015, pp. 395–415.

[8] Nee, V. W., and Kovasznay, L. S. G., "Simple phenomenological theory of turbulent shear flows," *Physics of Fluids*, Vol. 12, 1969, pp. 473–484.

[9] Baldwin, B., and Barth, T., "A one-equation turbulence transport model for high Reynolds number wall-bounded flows," *NASA Technical Memorandum*, 1990, pp. 102847, 1–20.

[10] Spalart, P., and Allmaras, S., "A one-equation turbulence model for aerodynamic flows," *Recherche Aérospatiale*, Vol. 1, 1994, pp. 5–21.

[11] Menter, F. R., "Eddy viscosity transport equations and their relation to the $k - \epsilon$ model," *J. Fluids Eng.*, Vol. 119, 1997, pp. 876–884.

[12] Yoshizawa, A., Abe, H., Matsuo, Y., Fujiwara, H., and Mizobuchi, Y., "A Reynolds-averaged turbulence modeling approach using three transport equations for the turbulent viscosity, kinetic energy, and dissipation rate," *Physics of Fluids*, Vol. 24, 2012, p. 075109.

[13] Hamba, F., "Exact transport equation for local eddy viscosity in turbulent shear flow," *Physics of Fluids*, Vol. 25, 2013, p. 085102.

[14] Menter, F. R., Egorov, Y., and Rusch, D., "Steady and unsteady flow modelling using the $k - \sqrt{k}L$ model," *Ichmt Digital Library Online*, Begell House Inc., 2006.

[15] Menter, F. R., and Egorov, Y., "The scale-adaptive simulation method for unsteady turbulent flow predictions. Part 1: theory and model description," *Flow, Turbulence & Comb.*, Vol. 85, 2010, pp. 113–138.

[16] Egorov, Y., Menter, F., Lechner, R., and Cokljat, D., "The scale-adaptive simulation method for unsteady turbulent flow predictions. Part 2: Application to complex flows," *Flow, Turbulence and Combustion*, Vol. 85, 2010, pp. 139–165.

[17] Abdol-Hamid, K. S., "Assessments of $k - kL$ Turbulence Model Based on Menter's Modification to Rotta's Two-Equation Model," *International Journal of Aerospace Engineering*, Vol. 2015, 2015, pp. 1–18.

[18] Jakirlic, S., and Maduta, R., "Extending the bounds of steady RANS closures: Toward an instability-sensitive Reynolds stress model," *International Journal of Heat and Fluid Flow*, Vol. 51, 2015, pp. 175–194.

[19] Hamba, F., "Nonlocal analysis of the Reynolds stress in turbulent shear flow," *Physics of Fluids*, Vol. 17, 2005, p. 115102.

[20] Heinz, S., "On mean flow universality of turbulent wall flows. I. High Reynolds number flow analysis," *Journal of Turbulence*, Vol. 19, 2018, pp. 929–958.

[21] Heinz, S., "On mean flow universality of turbulent wall flows. II. Asymptotic flow analysis," *Journal of Turbulence*, Vol. 20, 2019, pp. 174–193.

[22] Chin, C., Monty, J., and Ooi, A., "Reynolds number effects in DNS of pipe flow and comparison with channels and boundary layers," *International Journal of Heat and Fluid Flow*, Vol. 45, 2014, pp. 33 – 40.

[23] Sillero, J. A., Jiménez, J., and Moser, R. D., "One-point statistics for turbulent wall-bounded flows at Reynolds numbers up to $\delta^+ \simeq 2000$," *Physics of Fluids*, Vol. 25, 2013, pp. 105102,1–16.

[24] Vallikivi, M., Hultmark, M., and Smits, A. J., "Turbulent boundary layer statistics at very high Reynolds number," *Journal of Fluid Mechanics*, Vol. 779, 2015, pp. 371–389.

[25] Hoyas, S., and Jiménez, J., "Reynolds number effects on the Reynolds-stress budgets in turbulent channels," *Physics of Fluids*, Vol. 20, 2008, pp. 101511, 1–8.

[26] Abe, H., and Antonia, R. A., "Relationship between the energy dissipation function and the skin friction law in a turbulent channel flow," *Journal of Fluid Mechanics*, Vol. 798, 2016, pp. 140–164.

[27] Durbin, P. A., "Limiters and wall treatments in applied turbulence modeling," *Fluid Dyn. Research*, Vol. 41, 2009, pp. 012203, 1–18.

[28] Heinz, S., "Turbulent supersonic channel flow: direct numerical simulation and modeling," *AIAA Journal*, Vol. 44, 2006, pp. 3040–3050.